Cell Biol Toxicol (2014) 30:31–53
DOI 10.1007/s10565-013-9267-9

ORIGINAL RESEARCH

Alpha-Fe_2O_3 elicits diameter-dependent effects during exposure to an in vitro model of the human placenta

James J. Faust · Wen Zhang · Yongsheng Chen · David G. Capco

Received: 12 August 2013 / Accepted: 27 December 2013 / Published online: 25 January 2014

Abstract Iron oxide nanoparticles offer unique possibilities due to the change in their physico-chemical parameters when synthesized on the nanoscale (10^{-9} m) compared to their bulk forms. While novel uses exist for these materials when synthesized as nanoparticles, their unintended effects on the human body and specifically during pregnancy remain ill defined. In this study, an iron oxide nanoparticle, α-Fe_2O_3, was employed and the potential toxicity due to exposure was assessed in the widely used model human placental cell line BeWo b30. These cells were grown as epithelia, and subsequently assessed for their epithelial integrity, reactive oxygen species production and cellular viability, ultrastructural and morphological disruption, and genotoxicity as a result of exposure to α-Fe_2O_3 nanoparticles. Transepithelial electrical resistance indicated that exposure to the large (50 and 78 nm), but not small (15 nm) diameter particles of α-Fe_2O_3 nanomaterial resulted in leakiness of the epithelium. Exposure to the large diameters of 50 and 78 nm resulted in increases in cell death and reactive oxygen species. Disruption of junctional integrity as monitored by immunolocalization of the tight junction protein ZO-1 was found to occur as a consequence of exposure to large diameter NPs. It was found that there was reduction in the number of microvilli responsible for increased surface area for nutrient absorption after exposing the epithelia to large diameter NPs. Finally, genotoxicity as assessed by DNA microarray and confirmed by QPCR indicated that the large diameter particles (78 nm) induce apoptosis in these cells. These data indicate that large (50 and 78 nm), but not small (15 nm) α-Fe_2O_3 nanoparticles disrupt the barrier function of this epithelium as assessed by in vitro analysis.

Keywords α-Fe_2O_3 · BeWo · Genotoxicity · Hematite · Nanoparticle · Placenta

Abbreviations

BSA	Bovine serum albumin
DAPI	4′,6-Diamidino-2-phenylindole
DLS	Dynamic light scattering
ICB	Intracellular buffer
mRNA	Messenger RNA
NP(s)	Nanoparticle
PBS	Phosphate-buffered saline
ROS	Reactive oxygen species
SEM	Scanning electron microscopy
TEER	Transepithelial electrical resistance
TEM	Transmission electron microscopy
ZO-1	Zonula Occludens-1

Electronic supplementary material The online version of this article (doi:10.1007/s10565-013-9267-9) contains supplementary material, which is available to authorized users.

J. J. Faust · D. G. Capco (✉)
School of Life Sciences, Cellular and Molecular Biosciences, Arizona State University, Tempe, AZ 85287-4501, USA
e-mail: dcapco@asu.edu

W. Zhang
Department of Civil and Environmental Engineering, New Jersey Institute of Technology, Newark, NJ 07102, USA

Y. Chen (✉)
School of Civil and Environmental Engineering, Georgia Institute of Technology, Atlanta, GA 30332, USA
e-mail: yongsheng.chen@ce.gatech.edu

Background

Ferric oxide nanoparticles (NPs) stand at the cornerstone of molecular imaging (Amstad et al. 2011; Kievit and Zhang 2011) water remediation (Guo et al. 2007; Westerhoff et al. 2008), and industry (Zhou et al. 2002; Wu et al. 2006) due to the unique physico-chemical properties on the nanoscale (10^{-9} m) compared to their bulk forms. In this work, NP is defined on the basis of material diameter. Iron oxide NPs are commonly synthesized as crystals of α-Fe_2O_3, γ-Fe_2O_3, or Fe_3O_4 depending on their intended use. Furthermore, synthesis of small (e.g., <20 nm in diameter) iron oxide NPs such as γ-Fe_2O_3 result in production of superparamagnetic NPs, whereas those diameters synthesized >20 nm are antiferromagnetic (Gupta and Gupta 2005; GUPTA et al. 2007; Kievit and Zhang 2011; Wahajuddin 2012). This transition in diameter concomitant to a change in magnetism is underscored by the fact that these small diameters can be employed as a contrast agent during magnetic resonance imaging. In water systems, α-Fe_2O_3 NPs serve as sorbents for groundwater remediation (Blowes et al. 1997). Furthermore, in these water systems, α-Fe_2O_3 NPs were shown to be stable (He et al. 2008; Zhang et al. 2010; Zhang et al. 2012a). This investigation employed a model iron oxide NP, α-Fe_2O_3, whose physico-chemical parameters are well defined in the literature (He et al. 2008), and whose primary particle diameter can be controlled during synthesis (Zhang et al. 2010; Zhang et al. 2012b). Previous studies conducted in the Caco-2 cell model indicate that adsorption of α-Fe_2O_3 NPs is diameter-dependent (Zhang et al. 2010). For these reasons, the effects of exposure to α-Fe_2O_3 were subsequently assessed after exposure to an in vitro model of human syncytiotropoblasts, the cell barrier that interfaces maternal and fetal circulation in the placenta.

In eutherian mammals including humans, development of the fetus occurs inside the uterus of the mother. After fertilization, the embryo hatches from a glycoprotein rich matrix known as the zona pellucida and implants into the endometrial stroma of the mother (Aplin 1996). The first primitive epithelium of the embryo is known as the trophectoderm and later differentiation of the tissues takes place to form a placenta. The placenta parasitizes the circulatory system of the mother to supply the fetus with nutrients (Pijnenborg 1990). In humans the direct interface of the maternal blood supply with the embryo is a cell layer of cytotrophoblasts referred to as a syncytiotrophoblast. This single cell layer is underlain by cytotrophoblasts, basement membrane, and fetal capillaries which provide for a number of essential functions required for normal pregnancy including: nutrient and metabolite transport, immune function, gas exchange, and clearance of fetal waste and toxins (King 1992).

Due to the ethical limitations surrounding the use of, and availability of human tissues, investigators have relied on immortalized cell lines in order to study in vitro events such as implantation (Denker 1993; John et al. 1993; Grummer et al. 1994; Mardon et al. 2007; Hannan et al. 2010), syncytialization (Wice et al. 1990), drug, nutrient, oxygen (Rytting and Audus 2005; Bode et al. 2006; Rytting and Audus 2007; Rytting and Audus 2008; Morck et al. 2010), and NP transport (Kulvietis et al. 2011; Cartwright et al. 2012). The BeWo b30 cell line can be employed for these tasks and was subcloned from the parental cell line (Pattillo and Gey 1968; b30 is hereafter referred to as BeWo) to more closely resemble that of an in vivo trophoblast cell (van der Ende et al. 1987; van der Ende et al. 1990). While a number of studies have employed the BeWo model to assess the toxicity and transport of a variety of NPs, to our knowledge, there has yet to be a study assessing the potential effects of α-Fe_2O_3 NPs and a model for the human placenta (Saunders 2009; Menezes et al. 2011; Pietroiusti et al. 2013). Furthermore, the body of literature related to NP transport and toxicity during early fetal development remains ill-defined.

In a seminal study by Semmler-Behnke et al. (2007), it was shown that gold NPs can cross the placental barrier in rats after maternal intravenous or intratracheal administration and these NPs were found in fetal target organs (Semmler-Behnke et al. 2007; Semmler–Behnke et al. 2008). Studies conducted employing the mouse model through the combined use of inductively coupled plasma-mass spectroscopy (ICP-MS) and transmission electron microscopy (TEM) clearly demonstrated that NPs are found in the placenta, liver, and brain of developing pups after NP (SiO_2/TiO_2) administration through the maternal tail vein (Yamashita et al. 2011). Subcutaneous injection of TiO_2 NPs has been shown to cross the placenta and damage the genital and nervous system of developing pups (Takeda et al. 2009). Furthermore, studies employing the BeWo cell model demonstrated that fluorescent polystyrene NPs cross the placenta in a diameter-dependent fashion (Cartwright et al. 2012), NPs were able to induce DNA damage across BeWo

epithelial barrier (Bhabra et al. 2009), and this was subsequently found to be dependent on the barrier thickness (Huppertz 2011; Sood et al. 2011). For these reasons this study assessed the effects of a well characterized NP, α-Fe_2O_3, in the BeWo cell model in order to define the potential toxicity of these NPs in an in vitro model of the human placenta.

In this study, it was hypothesized that α-Fe_2O_3 NPs would have diameter-dependent effects upon in vitro exposure to a model human placental epithelium. If α-Fe_2O_3 NPs have diameter-dependent effects on the epithelium, then a number of predictions follow: (a) transepithelial electrical resistance (TEER) as a monitor of epithelia intactness will report differences in epithelial integrity after exposure to NPs of different diameters; (b) cellular viability as measured by Live/Dead® analysis and reactive oxygen species production will be directly influenced by the diameter of the NPs; (c) junctional integrity of the epithelium will be directly influenced by the diameter of the NPs; (d) morphological differences will accrue as a result of the diameter of the NP employed; and (e) genotoxicity will be influenced by the NP diameter.

Results

Large, but not small, non-functionalized α-Fe_2O_3 NPs disrupt BeWo epithelial integrity

If a population of NPs exist that exhibit diameter-dependent effects, it is anticipated that gross alterations in epithelia integrity will occur after exposure to NPs of different diameters. In order to test this, three different mean diameters of α-Fe_2O_3 NPs (small NPs defined as 15, and the large diameter NPs as 50 and 78 nm) were synthesized and subsequently employed, and each group displayed a narrow hydrodynamic diameter (Table 1). Diameters were confirmed by transmission electron microscopy (TEM; Fig. 1) each exhibiting a homogenous, colloidal NP population for each diameter tested. The physicochemical parameters of these particles have been extensively characterized elsewhere (He et al. 2008; Zhang et al. 2010; Zhang et al. 2012b), but briefly, a change in ζ-potential from positive to net negative as a result of incubation in medium containing supplements (i.e., fetal bovine serum and antibiotics) was observed as might be expected due to NP adsorption of serum components and/or the ionic strength of the culture medium (Kreuter 1994; Ehrenberg et al. 2009; Maiorano et al. 2010). Extensive characterization of these NPs with respect to time can be found in Supplemental Table 1.

As predicted, application of different NP populations (i.e., the small diameter of 15, and large diameters of 50, and 78 nm) resulted in significant changes in transepithelial electrical resistance (TEER) at a consistent mass concentration of 100 μg/mL (i.e., 33 μg/mm^2) for each diameter tested (Fig. 2a; see also Supplemental Figure 1 A). The mass concentration of 100 μg/mL was employed as a starting point since data concerning human exposure is limited and the effects of iron oxide NPs on the placenta are heretofore undefined (Saunders 2009; Sood et al. 2011). Furthermore, the concentration employed in this study is consistent with the concentrations employed in other studies (Buyukhatipoglu and Clyne 2011; Kalive et al. 2012), and during specialized imaging techniques (Mishra et al. 2010; Mahmoudi et al. 2011). It was found that the initial disruption (i.e., drop in TEER) occurred at 24 h after applying the NP-containing medium to the apical chamber of the Transwell® insert for large, but not small NPs. After 24 h epithelia exposed to both large populations of NPs (i.e., 50 and 78 nm) continued to decrease in TEER until the 5 day endpoint. At the 5-day endpoint, TEER was nearly half its original value for the epithelia exposed to large NPs. In contrast, it was found that both the untreated epithelia and those treated with 15 nm particles at

Table 1 The physico-chemical characteristics of α-Fe_2O_3 NPs of the three diameters: 15-, 50-, and 78-nm

Hydrodynamic diameter (DLS)	Diameter (TEM)	Polydispersive index	ζ-potential	ζ-potential standard deviation
15 nm	15 nm	0.3	−12 mV	26.8 mV
51 nm	50 nm	0.12	−7.5 mV	42.2 mV
94 nm	78 nm	0.25	−12.2 mV	18.5 mV

The narrow polydispersive index of the nanomaterial indicates a homogenous diameter of NPs. Zeta-potential measurements indicate uniformly stable, positively charged nanomaterial. All measurements were conducted in culture medium containing serum

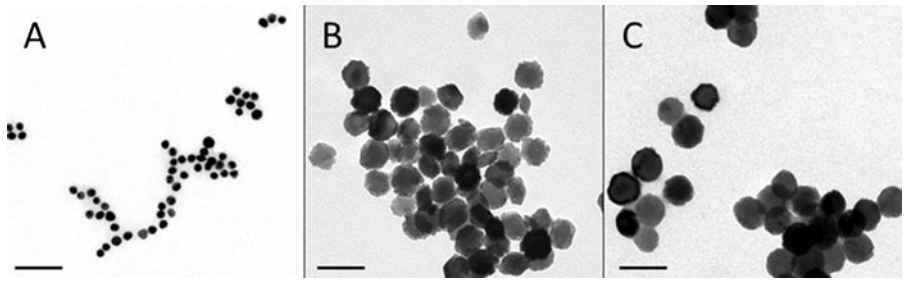

Fig. 1 TEM analysis of α-Fe_2O_3 NPs. TEM demonstrates a narrow distribution of the primary particle diameter for the nanomaterial employed in this study. **a** is the 15 nm NP. **b** is the 50 nm diameter and **c** is the 78 nm diameter. The *scale bar* is 100 nm

a concentration of 100 μg/mL maintained a high TEER throughout the experiment. In order to determine if application of NPs results in a permanent decrease in TEER a wash experiment was performed and terminal data (5 day endpoint) were assessed. It was found that untreated specimens had a significant, albeit modest increase in TEER at the 5-day endpoint. In this study, untreated was defined as those epithelia not exposed to nanomaterials at any time. However, epithelia treated with 15- and 78-nm α-Fe_2O_3 NPs and washed before 12 h resulted in no difference in TEER and a significant decrease in TEER, respectively (Fig. 2b). In the histogram, the gray and white bars correspond to the 12 h TEER value (gray bars) and the 5-day TEER endpoint value (white bars).

The dosimetry necessary to disrupt epithelial integrity for large NPs was subsequently assessed by titering down the concentration of 78 nm particles (Fig. 2c, d). It was found that exposure to 20-, but not 10 μg/mL concentrations of 78 nm NPs resulted in loss of TEER similar to the 100 μg/mL treated epithelia shown in Fig. 2a. This no-loss in TEER scenario of exposure below a mass concentration of 10 μg/mL was confirmed for all other diameters of NPs (Fig. 2d; see also Supplemental Figure 1 B).

Large diameter nanoparticles evoke increased reactive oxygen species (ROS) and cell death

In order to determine if the loss of epithelial integrity assessed as a change in TEER was due to cytotoxic mechanisms resulting in cell death, reactive oxygen species and subsequently cell death were investigated as a function of time. Under normal conditions (<10 cell per 1.4×10^5 μm^2), BeWo epithelia contained very few cells positive for reactive oxygen species as measured over the 1.4×10^5 μm^2 field of view in phase contrast, epifluorescent overlay micrographs (Fig. 3a, all micrographs are representative of 3.5×10^4 μm^2). BeWo epithelia were stimulated to produce reactive oxygen by the addition of 5 μM H_2O_2 overnight (8 h) supplemented into culture medium (Fig. 3b). Under these conditions, as a positive control for ROS, approximately 150 cells were positive for reactive oxygen species as measured by fluorescence of 2′,7′-dicholorofluorescein and this accounted for the majority of the total cells (220 cells per 1.4×10^5 μm^2). At both 1- and 3-days post treatment, the small diameter NP population (Fig. 3c, d) was not found to elicit large numbers of cells positive for ROS. However, a statistically significant difference between untreated and the 15 nm, 100 μg/mL-treated epithelia 1 day after exposure was noted (Fig. 3i). Further, both 50- and 78-nm diameter NPs at a concentration of 100 μg/mL after 1- and 3-days in culture showed a significant increase in cells positive for ROS (Fig. 3e–i).

If large-diameter NPs result in an increase in ROS, it might be expected that cell death occurs subsequent to this event. Cellular viability was assessed through the use of ethidium homodimer-1. Ethidium is a cell-

Fig. 2 TEER disruption is NP diameter as well as concentration dependent. **a** The graph illustrates the change in TEER after application of different diameters of α-Fe_2O_3 at a concentration of 100 μg/mL. Both 50- and 78 nm NP treated epithelia follow the same trend, whereas the 15-nm diameter exposure followed the trend of the untreated specimens. **b** Epithelial exposure to large-diameter NPs do not recover at the 5-day endpoint. The 12-h TEER value is shown in *gray* and the 5-day endpoint value is shown in *white*. **c** Application of 78 nm α-Fe_2O_3 at a mass concentration of 50- and 20 μg/mL appears to disrupt TEER. **d** Exposure to 10 μg/mL for all α-Fe_2O_3 diameters tested results in no change compared to the untreated specimens. As indicated in the "Methods" section, TEER levels off at its maximum value of 40 Ω cm^2 3 days after seeding BeWo cells. The NPs were applied after this 3-day culture period which is denoted as $t=0$ in the graphs. All experiments were conducted at least three independent times where $n=3$; *error bars* appear smaller than the data point marker for some points

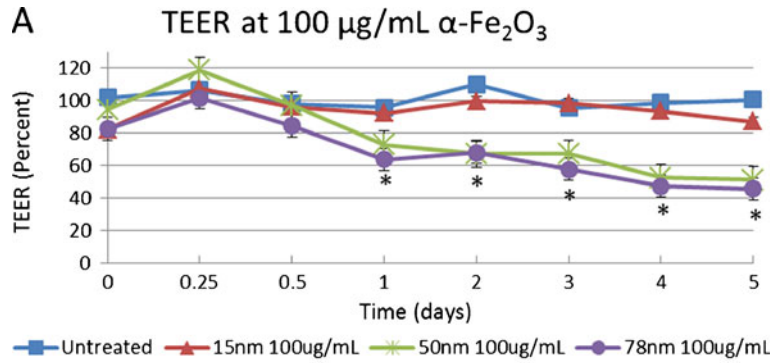
A
TEER at 100 µg/mL α-Fe2O3
TEER (Percent)
120
100
80
60
40
20
0
0
0.25
0.5
1
2
3
4
5
Time (days)
Untreated
15nm 100ug/mL
50nm 100ug/mL
78nm 100ug/mL

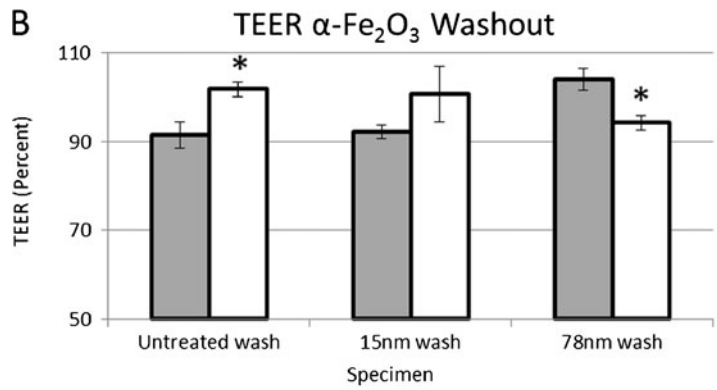
B
TEER α-Fe2O3 Washout
TEER (Percent)
110
90
70
50
Untreated wash
15nm wash
78nm wash
Specimen

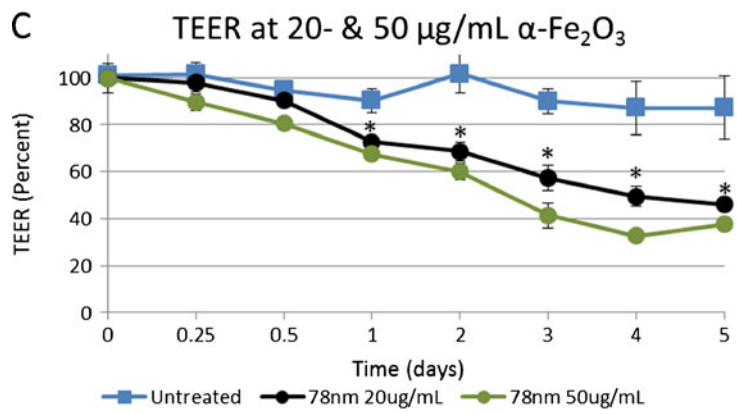
C
TEER at 20- & 50 µg/mL α-Fe2O3
TEER (Percent)
100
80
60
40
20
0
0
0.25
0.5
1
2
3
4
5
Time (days)
Untreated
78nm 20ug/mL
78nm 50ug/mL

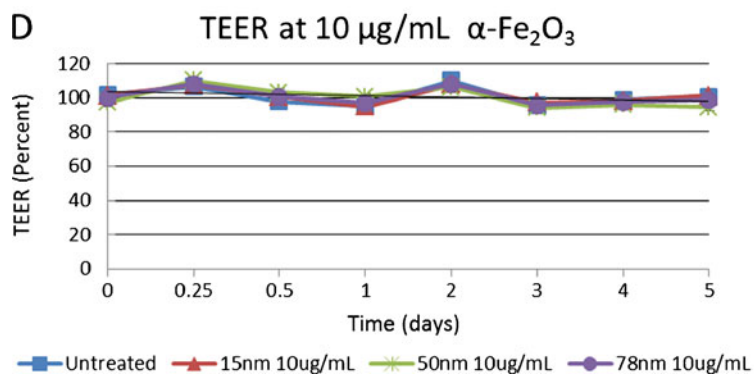
D
TEER at 10 µg/mL α-Fe2O3
TEER (Percent)
120
100
80
60
40
20
0
0
0.25
0.5
1
2
3
4
5
Time (days)
Untreated
15nm 10ug/mL
50nm 10ug/mL
78nm 10ug/mL

permeate probe, which upon nuclear-membrane disruption intercalates into DNA. Upon intercalation, ethidium undergoes a 40-fold increase in fluorescence, and this event can be monitored by an epifluorescent microscope. In this figure, 1.4×10^5 μm^2 was analyzed per micrograph, whereas 3.5×10^4 μm^2 was shown in order to permit adequate magnification. Under normal conditions, healthy BeWo epithelia at the 1 and 3 day time points analyzed as an area of 1.4×10^5 μm^2 had very few dead cells (1±1, 10±3, respectively; Fig. 4a, all micrographs shown are representative of 3.5×10^4 μm^2). Under conditions employed to assess maximal cell death, (a positive control for cellular death; saponin treatment), it was found that 217±6 cells died (Fig. 4b). Notable differences were found between the small (15 nm) and large (50 and 78 nm) NP treatments at a concentration of 100 μg/mL; there appeared to be a diameter-dependent increase in cell death (Fig. 4). After 1 and 3 days, epithelia treated with 15 nm particles were not significantly different from untreated epithelia (Fig. 4c, i). However, at both the 1 and 3-day time points, it was found that epithelia treated with 50 nm particles contained significantly more dead cells than untreated epithelia (Fig. 4e, f, i). Further, 78 nm treated epithelia also resulted in significantly more dead cells than untreated epithelia (Fig. 4g–i).

Large (78 nm) diameter α-Fe_2O_3 NPs disrupt intercellular tight junctions

Epithelial leakiness, as evidenced by the decrease in TEER, suggested the possibility of disruption of intercellular junction integrity. In order to test the prediction that the tight junctions, that must exist to maintain TEER, were disrupted as a result of NP exposure, a laser-scanning confocal approach was employed. It is well accepted that the apical localization of the tight junction protein ZO-1 labels intercellular tight junctions as well as indicating terminal differentiation of the epithelium (Anderson et al. 1989; Bement et al. 1993; Matter et al. 2005). Both the untreated and NP-treated specimens had a similar nuclear organization as evidenced by emission of the nuclear probe 4′,6-diamidino-2-phenylindole (DAPI; Fig. 5a, d). Analysis of the antibody to ZO-1 in untreated specimens demonstrated the conventional honeycomb arrangement of tight junctions surrounding each cell (Fig. 5b, c). However, after a 24-h exposure to α-Fe_2O_3 at a concentration of 100 μg/mL ZO-1 was disrupted with breaks in the continuous distribution of ZO-1 surrounding each cell (Fig. 5e, f). In some areas indicated by the white arrows ZO-1 was found to be completely absent though underlying nuclei (blue) were seen (Fig. 5e, f). It was found that the 15-nm-treated specimens were similar to the untreated, normal distribution of ZO-1 (Supplemental Figure 2).

The bulk of large (78 nm) diameter α-Fe_2O_3 NPs internalize through actin-mediated endocytosis, and accumulate at different cellular planes of the *z* axis as a function of time

Epithelial leakiness, as evidenced by a decrease in TEER, suggested the possibility of disruption of intercellular junction integrity. In order to test this as well as to assess the intracellular NP localization a TEM approach was employed. Untreated BeWo epithelia contained moderately polarized cells. Each cell had an electron-dense cytoplasm with numerous membrane-bound vesicle and organelles (Fig. 6a). After 4 h of incubation in NP-containing medium at a concentration of 100 μg/mL NPs were found internalizing apparently by a phagocytotic mechanism (Fig. 6b, c). Figure 6b shows membrane invaginations (white arrows) engulfing agglomerated NPs, whereas Fig. 6c shows a

Fig. 3 ROS analysis indicates that larger diameter α-Fe_2O_3 result ▶ in significant increases in ROS. At the 1-day time point, the epithelia had few cells positive for ROS (*green*) for every 1.4×10^5 μm^2 field of view that was observed (**a**). A positive control for ROS was conducted to illustrate high numbers of cells positive for reactive oxygen (**b**). After 1 day of exposure to the 15 nm NPs, a statistically significant increase is ROS was observed (**c**) and this number of ROS positive cells appears to decrease at the 3-day endpoint (**d**). **e** After 1 day of exposure to the 50-nm NPs, an increase in ROS was observed, and in contrast to the 15-nm specimens, this statistically significant increase was observed after 3 days as well (**f**). This increase in ROS at both 1 and 3 days was also observed for the 78-nm-treated specimens (**g**, **h**). **i** Quantification of the cells positive for ROS is shown in the histogram. In all the cases, data is shown as mean±standard error and $p<0.05$ was considered significant. Note that the histogram is shown as log-fold change on the *y* axis. The histogram represents 1.4×10^5 μm^2 of epithelium while the micrographs are representative of 3.5×10^4 μm^2 of the epithelium to permit adequate magnification. The *scale bar* is 50 μm. *Light gray boxes* indicate 1-day post-exposure, while *dark gray boxes* indicate 3 days post-exposure. The *white arrows* point to ROS puncta. All comparisons are made between untreated and NP-treated epithelia at their respective time points. All experiments were conducted at least three independent times

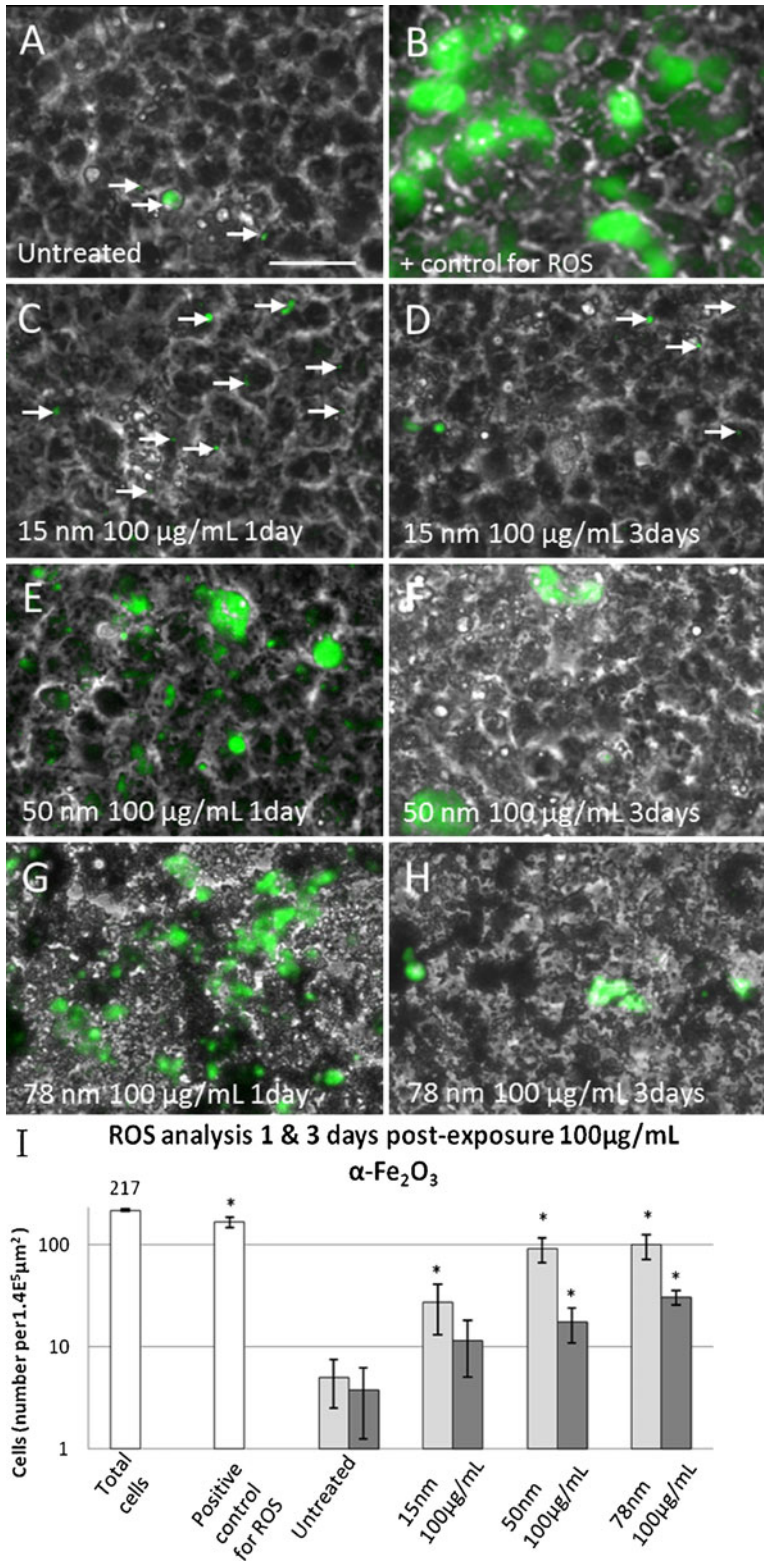
A
Untreated
B
+ control for ROS
C
15 nm 100 µg/mL 1day
D
15 nm 100 µg/mL 3days
E
50 nm 100 µg/mL 1day
F
50 nm 100 µg/mL 3days
G
78 nm 100 µg/mL 1day
H
78 nm 100 µg/mL 3days
I
ROS analysis 1 & 3 days post-exposure 100µg/mL
α-Fe2O3
Cells (number per1.4E5µm2)
217
100
10
1
Total cells
Positive control for ROS
Untreated
15nm 100µg/mL
50nm 100µg/mL
78nm 100µg/mL

similar event with NPs encapsulated in a vesicle (black arrows). Later, at the 8-h time point (Fig. 6d, e), NPs appeared to sediment and collect at the plasma membrane interface (Fig. 6d). Further, at this time point NPs were found concentrated at the lateral margins between cells (Fig. 6e). At the 16 h time point three distinct internalized populations of NPs were found (Fig. 7); that is, one population of large-diameter NPs was found enclosed within membrane bound vesicles (black arrows), another not membrane-bound (white arrows), and a third population seemed to be in a vesicle whose membrane appeared ruptured (white arrowheads; Fig. 7).

If large-diameter NPs are internalized by an actin-based mechanism (i.e., phagocytosis, macropinocytosis), then inhibiting actin polymerization should result in loss or decrease of large-diameter NP internalization. To test this prediction the fungal toxin Cytochalasin D, which is known to inhibit actin-mediated endocytosis (Silverstein et al. 1977) was employed during NP treatment. Figure 8a illustrates a representative cell that was exposed to neither Cytochalasin D nor NPs. Electron dense membranes are distinguishable, and the actin based projections known as microvilli are seen. Figure 8b indicated that NP agglomerates decorated the apical plasma membrane at 8 h of NP incubation in combination with Cytochalasin D incubation. However, after Cytochalasin D inhibition there appeared to be a small amount of NPs inside the cell and it appeared as if these NPs were not surrounded by membrane (Fig. 8c, black arrows). At the 8-h time point, and consistent with Figs. 7d, e and 8d, a number of NPs internalized in cells not treated with Cytochalasin D are shown.

Alpha-Fe_2O_3 NPs litter the apical brush-border and abolish the standing microvillar morphology

TEM analysis demonstrated that these NPs sediment to the epithelial surface in bulk over time in cell culture medium at the 8 h time point. If these large-diameter NPs result in effects that are deleterious to the cell, it might be expected that initial changes begin to occur at the cell-NP interface after NP touchdown. Thus, scanning electron microscopy (SEM) was employed to elucidate potential surface changes at this essential biological interface. In order to do this, a time-course experiment was conducted with replicate samples at a concentration of 100 μg/mL using the 78 nm diameter as the model large NP. The scanning electron micrographs in Fig. 9a–c illustrate the untreated brush-border at the apical surface of BeWo cells at 1, 3, and 5 days, respectively. Untreated, healthy BeWo cells had approximately 9 microvilli per square micrometer, and the number of microvilli appeared to extend to and remain at 11 microvilli per square micrometer over time (Fig. 9g). In contrast, micrographs of NP- treated epithelia (Fig. 9d–f) demonstrate a near complete effacement of the brush-border organization over the same time course. SEM analysis illustrated clusters of NPs littering the apical surface of BeWo epithelia (Fig. 9d–f, white arrow heads). After treatment with NPs, the total number of microvilli plummeted to fewer than 2 microvilli per square micrometer ($p<0.001$; Fig. 9g). Similar to the distribution of the untreated specimens, the number and morphology of the 15 nm treated specimens appeared to not be affected by exposure (Supplemental Figure 3).

Large (78 nm), but not small (15 nm), α-Fe_2O_3 NPs elicit cellular changes at the level of the gene

The experiments conducted in the aforementioned text indicate cellular changes as a result of NP exposure. In order to investigate the potential that α-Fe_2O_3 NPs evoke a response in gene expression, a genome-wide DNA microarray approach was employed. Through the use of Agilent human 44 K arrays, it was found that epithelia treated with 78 nm α-Fe_2O_3 at a mass

Fig. 4 Live/dead analysis of BeWo epithelia as assessed by phase contrast, fluorescence overlay micrographs indicate cell death after exposure to large-diameter α-Fe_2O_3 NPs. At 1 day healthy epithelia have about 1 dead cell (*red*) per 1.4×10^5 μm^2 field of view was observed in both control specimens (**a**). A positive control for cell death was conducted to illustrate ethidium fluorescence in the nuclear area of most cells in the epithelium (**b**). After 1 day and 3 days post-exposure to 15 nm NPs (**c**, **d**), there was no significant difference compared to controls (**a**). **e** After 1 day of exposure to the 50-nm NPs, an increase in cell death was observed, and this number was consistent at the 3-day time point (**f**). Furthermore, those epithelia exposed to the 78-nm diameter NPs had a high number of dead cells. **i** Quantification of cell death is shown in this histogram. In all the cases, data is shown as mean±standard error and $p<0.05$ was considered significant. Note that the histogram is shown as log-fold change on the *y* axis. The histogram represents 1.4×10^5 μm^2 of epithelium while the micrographs are representative of 3.5×10^4 μm^2 of the epithelium to permit adequate magnification. The *scale bar* is 50 μm. *Light gray boxes* indicate 1 day post-exposure, while *dark gray boxes* indicate 3 days post-exposure. All comparisons are made between untreated and NP-treated epithelia at their respective time points. All experiments were conducted at least three independent times

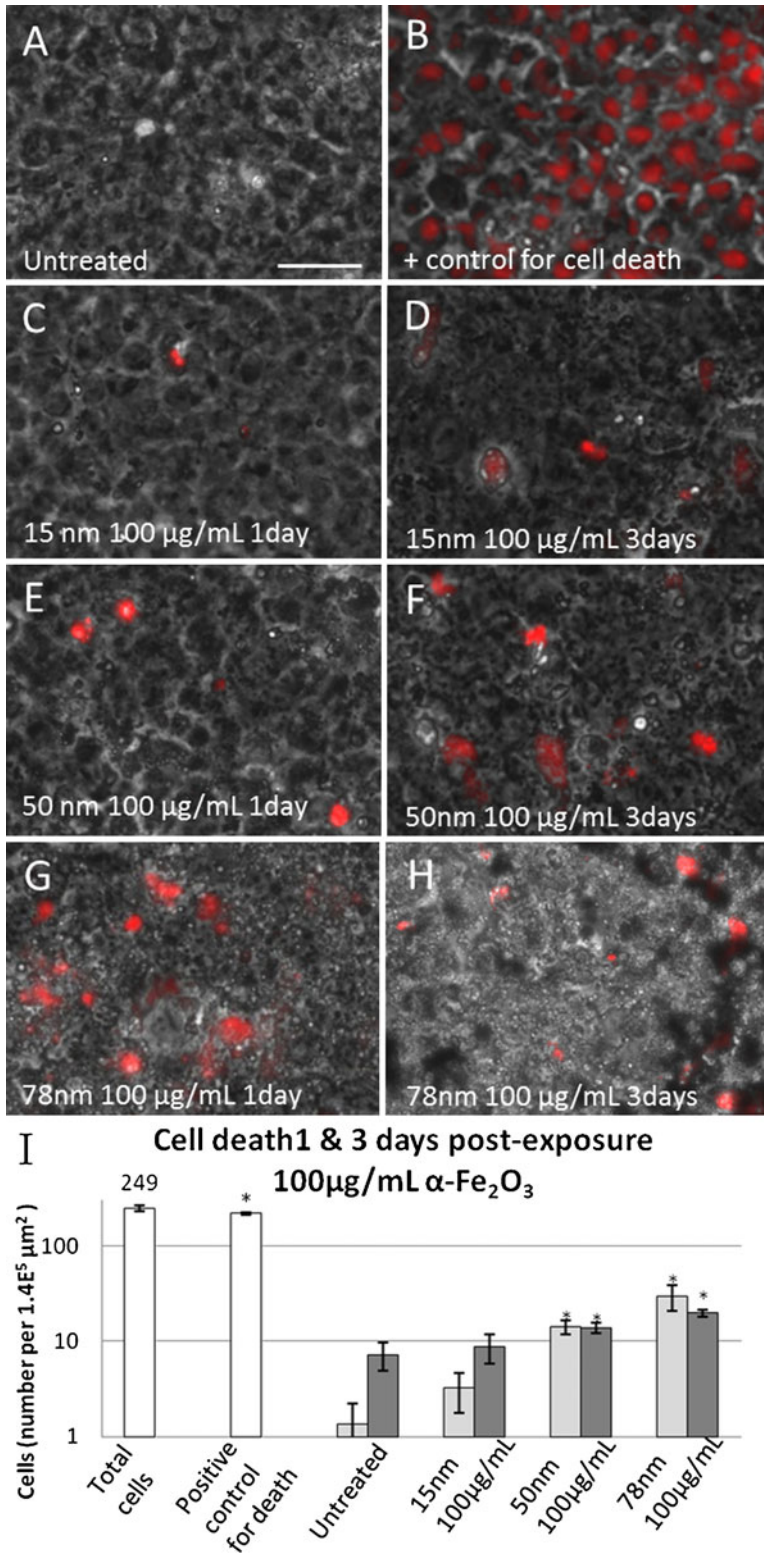
A
Untreated
B
+ control for cell death
C
15 nm 100 µg/mL 1day
D
15nm 100 µg/mL 3days
E
50 nm 100 µg/mL 1day
F
50nm 100 µg/mL 3days
G
78nm 100 µg/mL 1day
H
78nm 100 µg/mL 3days
I
Cell death1 & 3 days post-exposure
100µg/mL α-Fe2O3
249
Cells (number per 1.4E5 µm²)
100
10
1
Total cells
Positive control for death
Untreated
15nm 100µg/mL
50nm 100µg/mL
78nm 100µg/mL

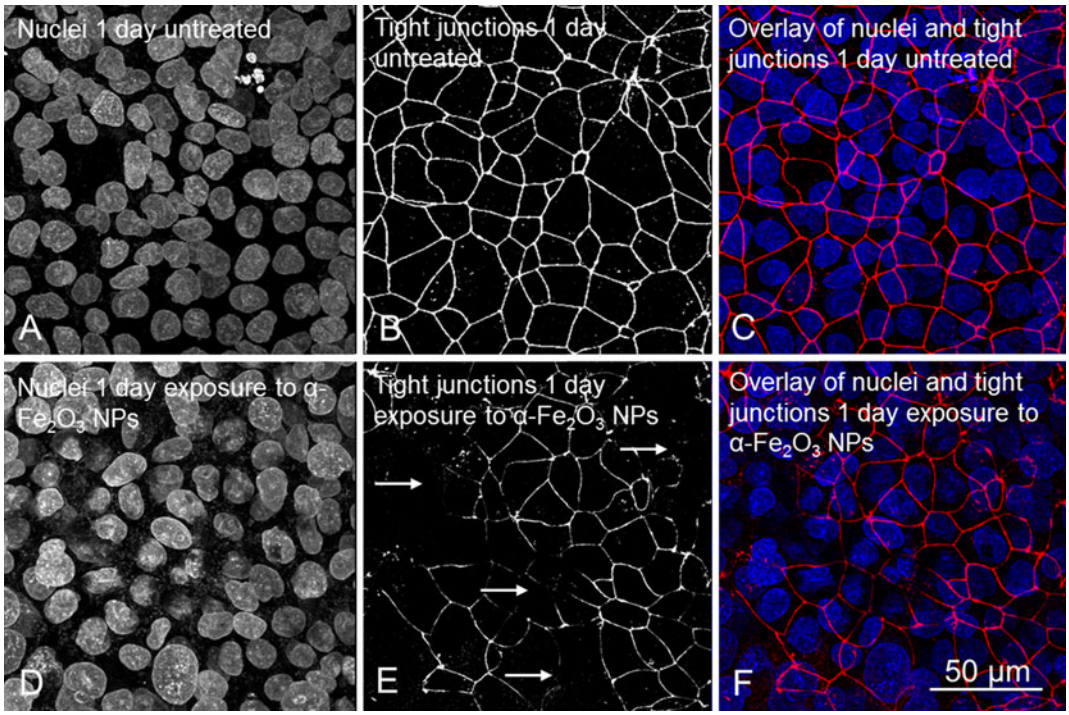

Fig. 5 Tight junctions, as measured by ZO-1 immunofluorescence, are perturbed in 78-nm-treated specimens. **a** Untreated, healthy BeWo epithelia display the typical honeycomb arrangement of ZO-1 at the intercellular junctions and this appears contiguous across the epithelium. **b** After a 24-h exposure to 78 nm α-Fe_2O_3 at a concentration of 100 μg/mL, tight junctions are disrupted. The distribution of ZO-1 is non-contiguous throughout the epithelium, and in some areas, ZO-1 appears absent (*white arrows*). All specimens were images through the entire *z* axis at 0.5 μm increments and shown are maximum projection images. In both the untreated and NP-treated specimens, the epithelia were treated as replicate samples and grown for 3 days prior to NP exposure. The *scale bar* is shown in **f**

concentration of 100 μg/mL for 72 h resulted in statistically significant ($p \leq 0.05$) changes in 799 genes. In contrast, epithelia treated with 15 nm α-Fe_2O_3 at a mass concentration of 100 μg/mL for 72 h were found to have no statistically significant changes (Fig. 10). In this study a fold-change cutoff of ±2.0 was selected consistent with other reports (Mutch et al. 2002; Quackenbush 2002). Concerning the 78-nm NP exposure, of the 799 genes that were changed, it was found that 589 genes were upregulated and 210 genes were downregulated. Through the use of GeneSpring (Agilent) these numbers were narrowed and genes that potentially explain epithelial integrity were further interrogated. Downregulated genes (Table 2) included 2 broad categories: "Tight junctions," and "adherens junctions." It was found that claudin 19 was suppressed 4.82-fold, as well as a number of protocadherins which are known to be expressed during early development (Rampon et al. 2008; Kokkinos et al. 2010) had fold-changes ranged from −2 to −7. Upregulated genes (Table 3) included those involved in actin-binding (actin associated), the cytoskeleton, and apoptosis. It was found that the expression of α-actinin 1 and 3 were enhanced by 2.10 and 2.80, respectively. *CapZ* mRNA which encodes the actin filament capping protein was upregulated 5.80-fold. Three other actin associated genes were found upregulated from 3.65 to 4.62 and those include genes encoding dynamin, twinfilin, and tropomyosin. Gamma-actin was found upregulated 3.33-fold and Keratin 8 and 83 were 6.66 and 9.86-fold increased compared to untreated specimens, respectively. Twelve genes were found upregulated and associated with apoptosis and those include: Caspase 3 (2.80), caspase 8 (5.36), programmed cell death 6 (3.89), tumor necrosis factor (TNF) associated factor 2 (3.69), TNF receptor 5 (2.39), death associated protein (DAP; 4.59) TNF receptor 12A (2.88), foxo4 (4.16), heat shock protein 90 A (4.73) BCL2-like 1 (2.18), and death inducer-obliterator 1(3.06).

In keeping with the microarray analysis described in the preceding text, quantative-RT-PCR (QPCR) analysis demonstrated that *CASP8*, and *TNFRSF12A*, had similar expression (Fig. 11).

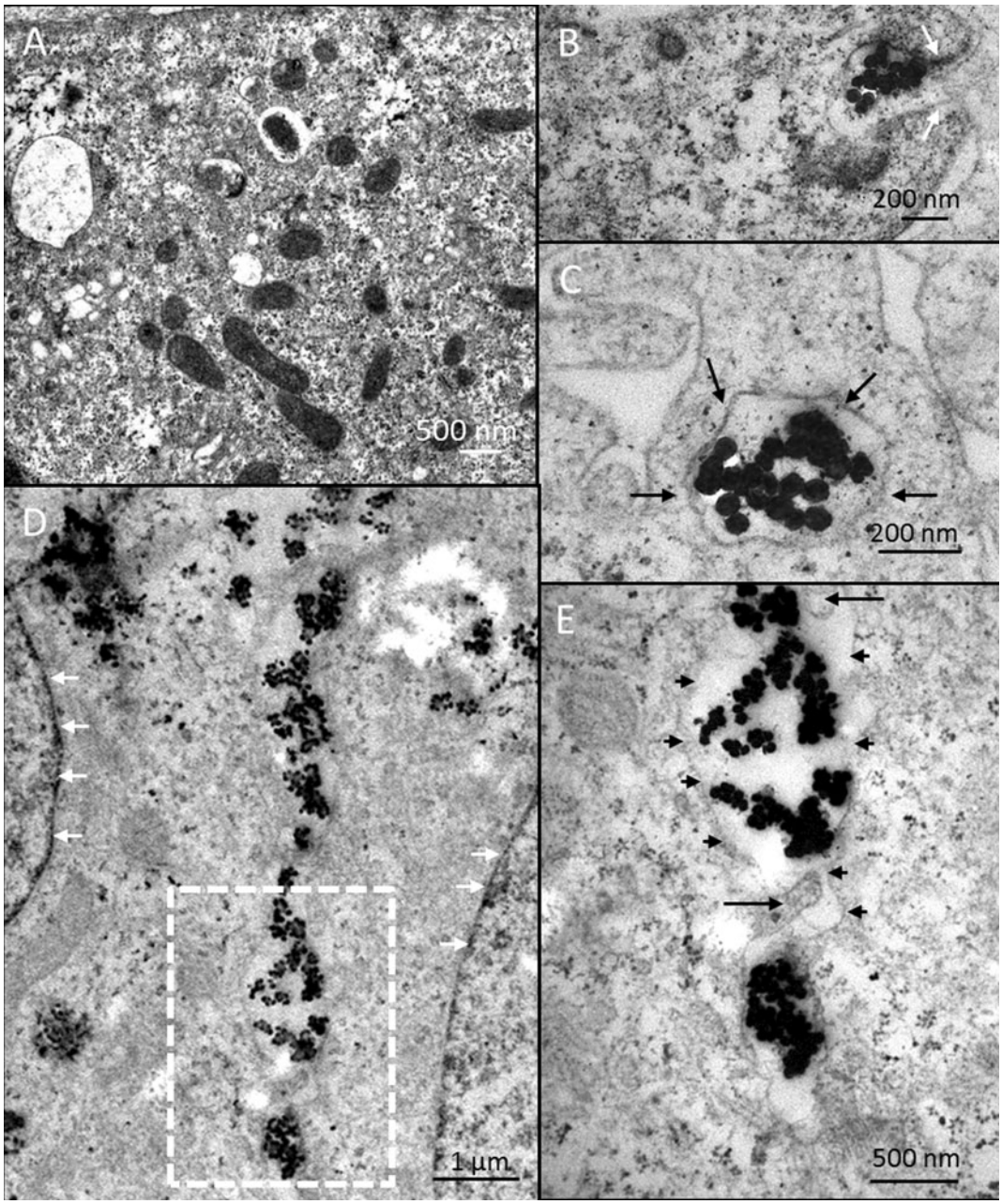

Fig. 6 TEM analysis of intra- and extracellular NP localization in BeWo epithelia. **a** Numerous endocytotic, secretory granules, and electron dense mitochondria can be seen in untreated BeWo epithelia. **b** After a single 4-h exposure to the 78 nm α-Fe_2O_3 NPs at 100 μg/mL, these NPs can be seen in the extracellular space and beginning to endocytose via large membrane invaginations that surround agglomerated NPs. The *white arrows* point to large membrane protrusions surrounding NPs. **c** At 4 h, the NPs appear to be contained in membrane-bound vesicles at the apical region of the cells. The *black arrows* point to the electron-dense membrane surrounding the NPs. **d** After 8 h in culture, NPs are seen in the lateral margins between two cells. The *white arrows* point to the two different nuclei. **e** The micrograph represents a magnification of the region of interest shown as a *white box* in **d**. NPs can clearly been seen as non-membrane-bound and further interdigitating microvilli are present between the two cells. The *black short arrows* point to the membrane of the cell, while the *long black arrows* point to interdigitating microvilli. The *scale bars* are shown at the *lower right* corner of each micrograph

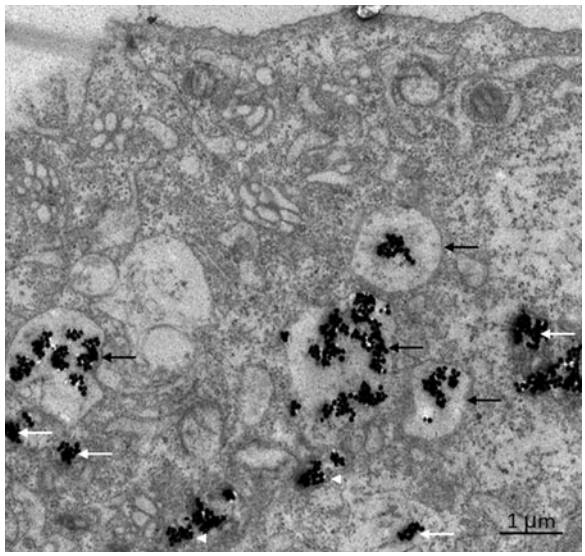

Fig. 7 NPs represent at least three discrete "populations" of intracellular NPs. After 16 h of exposure to 78 nm α-Fe_2O_3, NPs appear as three discrete populations, that is, some NPs appear clearly membrane-bound as indicated by *black arrows*. The second population of NPs appear non-membrane-bound (*white arrows*). The third group are in vesicles that may be rupturing (*white arrowheads*). The *scale bar* is shown at the *lower right* corner of each micrograph (1 μm)

Discussion

A principal finding in this study is that the diameter of a nanomaterial (α-Fe_2O_3) elicits differential effects ranging from lethal to almost no effect in an established model of the human placental epithelium based on the criteria described in the text below. This investigation showed that the large α-Fe_2O_3 NP diameters tested (50, and 78 nm) deleteriously affect this placental epithelium, while the small diameter NP (15 nm) exhibited relatively fewer effects in this model system within the context of points 1–4 described in the text below. This

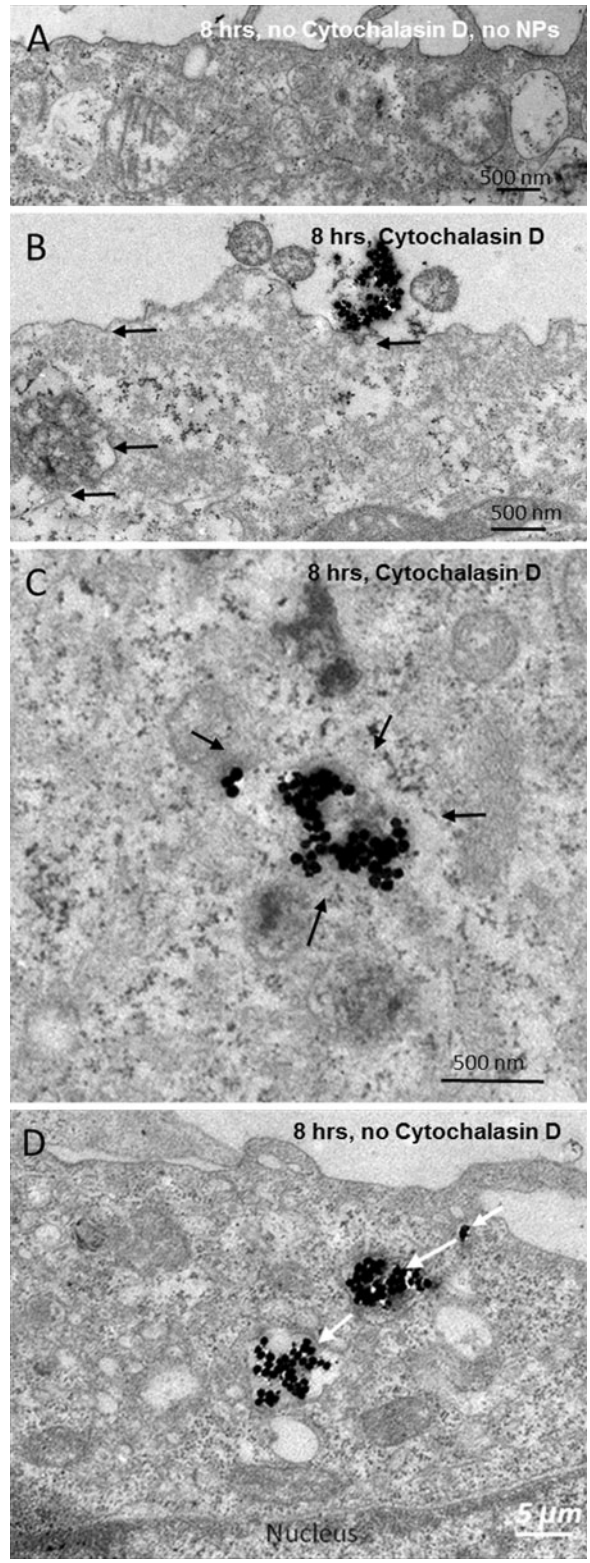

Fig. 8 NP internalization is largely, but not completely, inhibited ▶ by disruption of actin-mediated endocytosis. **a** Untreated specimens have clearly distinguishable membrane-bound vesicles with apical microlli projections. **b** After treatment with Cytochalasin D for 1 h prior to, and during the duration of NP exposure (8 h) NP endocytosis appears to be disrupted. *Black arrows* point to clearly identifiable cell membranes. The nanoparticle agglomerates appear to decorate the apical surface of the cells. **c** Low levels of NPs appear internalized at this time point (8 h.). However, electron-dense membranes surrounding the NPs were not clearly observed. **d** When the NPs are dosed without Cytochalasin D inhibition of actin, there appears many more internalized NPs. The *white arrows* point to the NPs. The *scale bars* are in the *lower right* corner of each micrograph

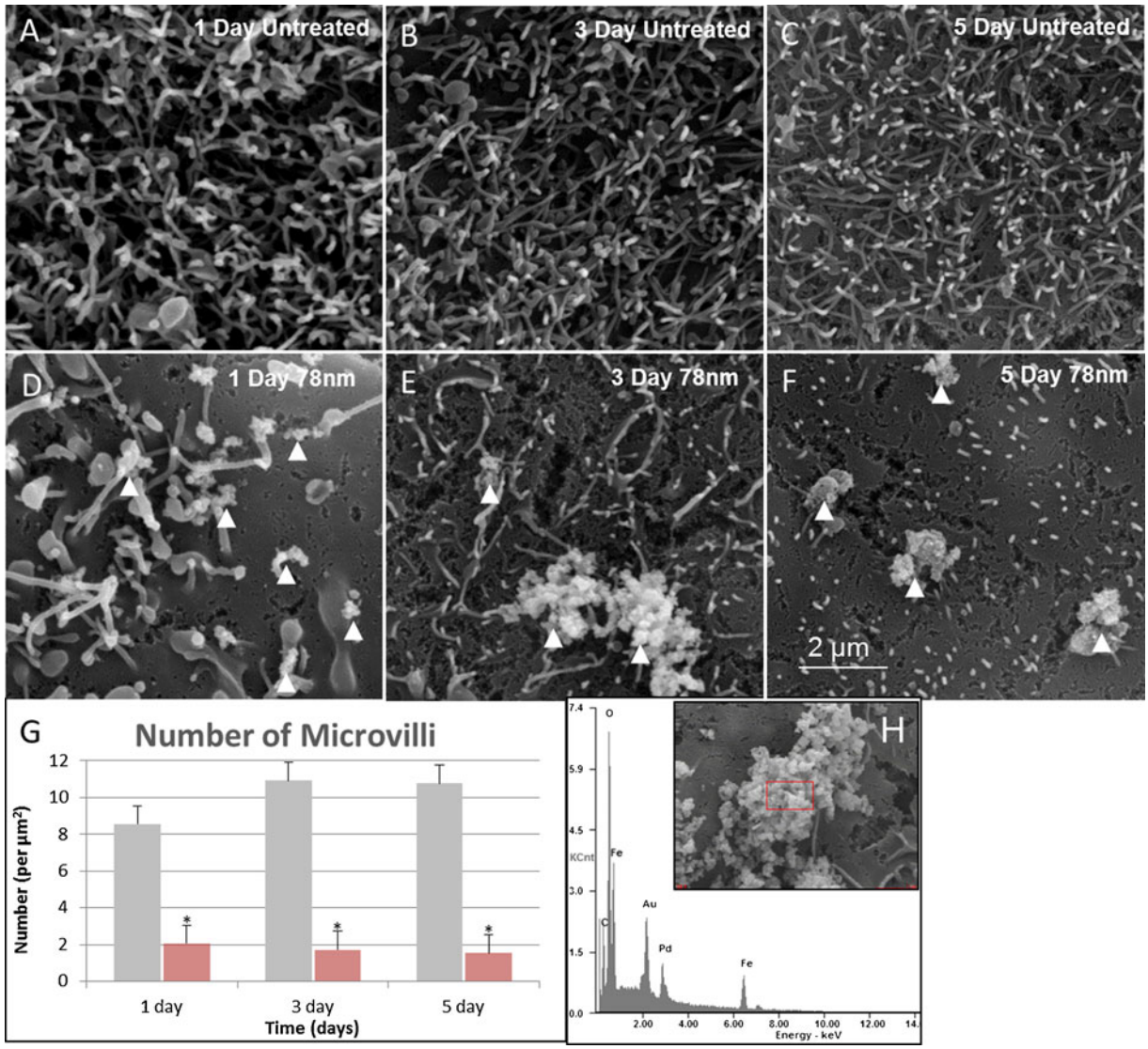

Fig. 9 Scanning electron microscopy reveals the effects on the brush-border of BeWo cells. **a**–**c** In untreated cells, there are well-developed microvilli on the apical surface at days 1, 3, and 5, respectively. **d**–**f** However, after treatment with α-Fe_2O_3 NPs, the apical brush-border is nearly abolished ($p<0.001$). The *arrowheads* point to NP clusters. **g** The histogram shown quantitation of microvilli. The number of microvilli is significantly fewer as a result of NP exposure. Each image was taken at identical magnification and thus the *scale bar* in **f** (2 µm) can be compared across micrographs. *Error bars* represent mean±standard error. No fewer than 5 micrographs were scored representing five randomly chosen areas of 1 µm^2 per micrograph in four independent experiments

investigation clearly showed, through the use of four orthogonal techniques, that the epithelium was disrupted as a result of exposure to the large (78 nm), but not small (15 nm), α-Fe_2O_3 NP diameter: (a) TEER measurements as an indication of epithelial integrity (Claude 1978; Hidalgo et al. 1989; Koeneman et al. 2009) indicated that large, but not small diameter α-Fe_2O_3 NPs disrupt the "intactness" of the epithelium. (b) At the protein level through the use of antibodies directed against ZO-1, it was shown that these α-Fe_2O_3 NPs disrupted the normal arrangement of ZO-1 for large, but not small α-Fe_2O_3 NPs. (c) The microarray analysis indicated gross changes in gene expression for large, but not small NPs. (d) Finally, ultrastructural and morphological changes were observed after exposure to large, but not small α-Fe_2O_3 NPs.

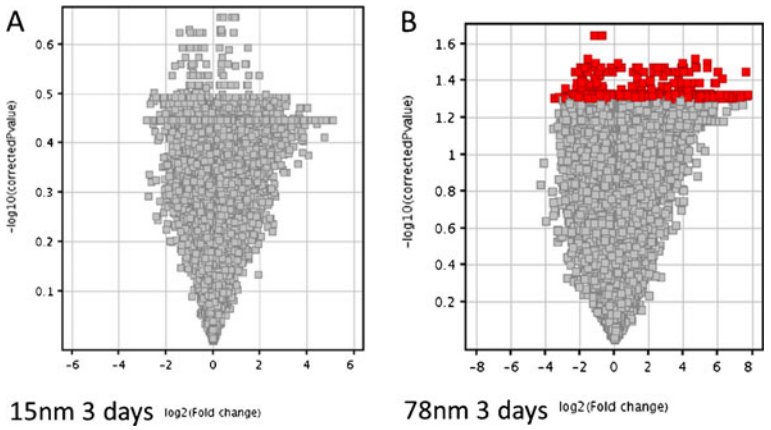

Fig. 10 DNA microarray analysis indicates that exposure to 78 nm α-Fe_2O_3 evokes statistically significant changes at the level of the gene at 72 h post-exposure. **a** The volcano plot indicates that exposure to 15 nm α-Fe_2O_3 NPs only slightly changes the fold-expression of any number of 44,000 genes, none of which are statistically significant. **b** Exposure to the 78 nm diameters results in a number of statistically significant ($p \leq 0.05$) changes in expression (*red*). The experiment was conducted as biological triplicate on the same day

The trophoblast layer in eutherian mammals including humans forms the interface between the mother and the developing fetus (Saunders 2009), and further acts as a selective physiological barrier (King 1992). The data presented in this report suggest that there are two routes acting in concert to disrupt the barrier function of the epithelium. The first route of epithelial disruption can be attributed to a loss of the intercellular tight junctions. In this study, it was shown that as early as 12 h in culture, TEER begins to drop and this drop does not appear to be recoverable after exposure to large NPs. In addition, laser scanning confocal analysis demonstrated that exposure to large, but not small NPs disrupted the normal arrangement of ZO-1, an established marker for tight junctions (Stevenson et al. 1986; Furuse et al. 1994). Ultrastructural analysis indicated that NPs accumulate in the lateral margins between cells. Finally, at the mRNA level the claudin 19 gene whose protein product is known to bind ZO-1 and permit tight junction assembly (Lee et al. 2006), was downregulated ~5-fold. Debate has arisen within the scientific community as to the reliability of TEER measurements (Jovov et al. 1991; Mukherjee et al. 2004). In particular, a number of factors are known to affect TEER measurements. In this study, TEER was found to be similar in magnitude to those values reported elsewhere (Cartwright et al. 2012). Further, in this study, the temperature was controlled for by equilibrating the epithelia to room temperature before conducting the measurements (see the TEER subheading in the "Methods" section for the experimental details). While much of this work was contingent on the interpretation of the TEER results, the orthogonal techniques of immunocytochemistry and TEM clearly supported these data. Indeed, during the initial drop in TEER ZO-1 localization as an indicator of tight junctions was found to be disrupted after exposure to the large diameter NP (78 nm; Fig. 5). Furthermore, TEM analysis indicated that

Table 2 Microarray analysis indicates that 78 nm α-Fe_2O_3 NPs elicit downregulation of mRNA encoding proteins responsible for intercellular junctions

Relevance	GenBank Accession	Gene	Description	Fold-change
Tight junctions	[NM_148960]	*CLDN19*	Claudin 19	−4.82
Adherens junctions	[NM_015669]	*PCDHB5*	Protocadherin α5	−7.36
	[NM_018930]	*PCDHB10*	Protocadherin α10	−4.30
	[NM_018932]	*PCDHB12*	Protocadherin α12	−3.87
	[NM_018933]	*PCDHB13*	Protocadherin α13	−2.03
	[NM_018934]	*PCDHB14*	Protocadherin β14	−4.69
	[NM_032101]	*PCDHGB7*	Protocadherin αb,7	−3.64

Exposure to 78 nm α-Fe_2O_3 NPs at a concentration of 100 μg/mL results in downregulation of genes essential for junctional integrity at the 3-day time point. Claudin 19, a component of tight junctions is downregulated nearly 5-fold. In addition, a number of protocadherins are downregulated ranging from 2- to 7-fold. All data shown represent specimens conducted as biolgical triplicate where $p \leq 0.05$

Table 3 Microarray analysis indicates that 78 nm α-Fe_2O_3 NPs upregulate gene involved in apoptosis, and actin bundling and organization

Relevance	GenBank Accession	Gene	Description	Fold-change
Actin associated	[NM_001102]	*ACTN1*	Actinin, alpha 1	+2.10
	[NM_001104]	*ACTN3*	Actinin, alpha 3	+2.80
	[NM_006135]	*CAPZA1*	Action Capping Protein	+5.80
	[NM_001043352]	*TPM3*	Tropomyosin 3	+4.32
	[NM_007284]	*TWF2*	Twinfilin homolog 2	+4.90
	[NM_004723]	*ARHGEF2*	Rho/Rac GEF 2	+3.37
	[NM_001005360]	*DNM2*	Dynamin	+3.65
Cytoskeleton	[NM_001614]	*ACTG1*	Actin, Gamma	+3.33
	[NM_002273]	*KRT8*	Keration 8	+6.66
	[NM_002282]	*KRT83*	Keration 83	+9.86
Apoptosis	[NM_004346]	*CASP3*	Caspase 3	+2.80
	[NM_033358]	*CASP8*	Caspase 8	+5.36
	[NM_013374]	*PDCD6IP*	Programmed cell death 6	+3.89
	[NM_021138]	*TRAF2*	TNF associated factor 2	+3.69
	[NM_001250]	*CD40*	TNF receptor 5	+2.39
	[NM_004394]	*DAP*	Death associated protein	+4.59
	[NM_016639]	*TNFRSF12A*	TNF receptor 12A	+2.88
	[NM_005938]	*FOXO4*	Forkhead	+4.16
	[NM_019885]	*CYP26B1*	Cytochrome P450 B1	+3.76
	[NM_007355]	*HSP90AB1*	Heat shock protein 90 A	+4.73
	[NM_138578]	*BCL2L1*	BCL2-like 1	+2.18
	[NM_022105]	*DIDO1*	Death inducer-obliterator 1	+3.06

Exposure to 78 nm α-Fe_2O_3 NPs at a concentration of 100 μg/mL results in upregulation of genes essential for actin organization and bundling such as CapZ, γ-actin, among others. Apoptosis appears to be the cause of cell death as initiator and executor caspases are upregulated as well as the receptors responsible for their activation. All data shown represent specimens conducted as biological triplicate where $p \leq 0.05$

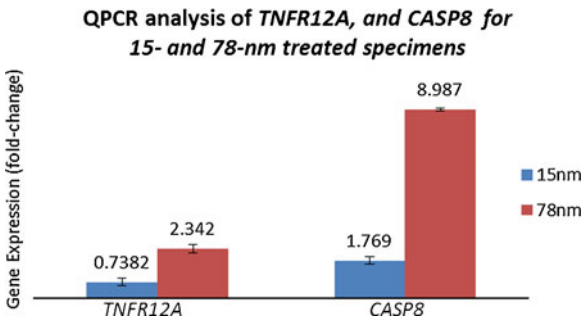

Fig. 11 QPCR analysis of cDNA employed during microarray analysis has a similar expression profile for *TNFR12A* and *CASP8*. Similar results to those obtained during microarray analysis show that 15 nm exposed specimens show modest changes in expression, whereas epithelia exposed to the 78 nm diameter have large changes in gene expression. *Error bars* represent standard deviation. Relative gene expression was normalized by the α-tubulin housekeeping gene *TUBA1A* and calculated by the ΔΔCt method. *Error bars* are shown as mean±SD. Experiments were conducted as technical triplicates on the same day

NP agglomerates (78 nm) were found distributed between the lateral margins of cells (Fig. 6d, e). Since TEER is effectively a measure of the integrity of the tight junctions (Blume et al. 2010), and the orthogonal techniques indicated a disruption of the tight junctions during the time there was a drop in TEER, these data are well supported.

An alternative route to disrupt the barrier function can be accredited to "holes" in the epithelium as a result of cell death. This study tested if the diameter of the α-Fe_2O_3 NP affects the viability of the epithelium and it was found that large, but not small α-Fe_2O_3 NPs induced cell death as measured by ethidium-homodimer nuclear fluorescence at both 1 and 3 days of NP exposure. Cell death can be attributed to a number of mechanisms (Ellis et al. 1991); however, evidence (described in the subsequent paragraph) was presented in this study to suggest that cell death is of the apoptosis variety.

Concerning apoptosis two signaling mechanisms by which the cell can commit suicide exist (Reed 2000; Thorburn 2004; Fulda and Debatin 2006). The extrinsic pathway can be stimulated by extracellular signaling ligands that bind to integral membrane death receptors (Nagata 1997; Thorburn 2004). This ligand-receptor interaction causes a conformational change in the protein and permits establishment of a molecular scaffold known as the death-inducing signaling complex (DISC; Thorburn 2004). Caspase 8 is a molecular component of the DISC and upon its release from the DISC has the potential to activate the executioner caspase, caspase 3 (Fischer et al. 2003).

Genome-wide analysis through the use of DNA microarray employed during this study indicated that epithelia exposed to large diameter NPs (78 nm) at the same concentration and exposure duration as the 15 nm specimens elicited a statistically significant ($p \leq 0.05$; $n=3$) increase in the expression of these pro-apoptotic genes. Indeed, this study showed that those molecular components at the mRNA level are upregulated corresponding to the extrinsic pathway of cell induced apoptosis (Table 3). In addition, it was found that mRNA encoding two receptors of TNFα were upregulated as well as both caspase 8 and caspase 3. In contrast, it was found that there were no statistically significant changes in gene expression after exposure to the 15-nm α-Fe_2O_3 NPs at a concentration of 100 μg/mL.

The data presented in this report shows that there are notable changes in the number of cells positive for reactive oxygen species after treatment with these NPs at both 1 and 3 days post-exposure. Moreover, it is a known phenomenon that NPs are able to "escape" endosomes (Verma and Stellacci 2010). The transmission electron micrographs shown in this study appear to contain some agglomerated intracellular NPs that have no indication of electron-dense membranes surrounding the NPs. It is known that iron oxide NPs elicit the production of ROS and furthermore rupture of the lysosome as might be the case for the apparently non-membrane bound NPs found in this study (Buyukhatipoglu and Clyne 2011). This increase in intracellular ROS could "jumpstart" a signaling cascade for apoptosis.

Apoptosis is not the only effect of NPs on cells, subtle effects of NPs on the biology of the cells and tissues have also been reported. The first paper to describe what was then referred to as "subtle" effects of NP exposure demonstrated that NPs (a 70/30 % mixture of rutile and anatase TiO_2) efface the brush-border of intestinal enterocytes in vitro in a dose-dependent manner (Koeneman et al. 2010; Faust et al. 2012). Subsequent studies employing α-Fe_2O_3 NPs by Zhang et al. (2010) and later Kalive et al. (2012) at concentrations ranging from 1 to 300 μg/mL showed a similar microvillar disruption as a result of NP exposure (Zhang et al. 2010; Kalive et al. 2012). In the present study a number of structural proteins related to actin bundling (tropomyosin and α-actinin) were found to be upregulated after exposure to large NPs. Furthermore the actin capping protein CapZ, which is a known constituent of the apical region of the microvillus in placental cells (Heintzelman et al. 1994), was found to have a 5-fold increase in mRNA expression in the present study. This apical region referred to as the plus-tips of the microvillus appears in electron micrographs as an electron dense region and was shown to be the organization center from which microfilaments emanate during morphogenesis (Mooseker 1985; Berryman et al. 1995). These data indicate a change in the normal actin-bundling properties of the trophoblast epithelium and suggest that at the mRNA level actin capping as a means to promote actin disassembly may be the mechanism driving the loss of microvilli in this cell system at the protein level.

Conclusion

In the present investigation, it was hypothesized that α-Fe_2O_3 NPs elicit diameter-dependent effects in an in vitro model of the human placenta. From this, it would be predicted that if the diameter of the NP affects the viability of the epithelium then exposure to different diameters would affect the epithelium in different ways. This study showed that the large diameters of 50- and 78-nm αFe_2O_3 disrupted the junctional integrity of the epithelium and subsequently resulted in apoptosis, whereas the smaller diameter of 15 nm appeared to have little effect on the epithelium and did not show those gross changes observed after exposure to large diameters. Since the fetal/maternal interface is responsible for selectively shuttling nutrients to the placenta, acting as a barrier to the mother's immune components, and permitting waste and gas exchange, junctional disruption or apoptosis of these cells could result in pregnancy complications, or result in fetal malnutrition. Future studies will interrogate the signaling events responsible for apoptosis at the protein level as this remains to be elucidated.

Methods

Synthesis of α-Fe_2O_3 NPs

All α-Fe_2O_3 NPs were synthesized by Dr. Wen Zhang in the laboratory of Dr. Chen at Georgia Institute of Technology according to the method of Penners and Koopal (Penners and Koopal 1986; Zhang et al. 2011; Zhang et al. 2012b). Briefly, 20 mM $FeCl_3$ in 4 mM HCl solution was incubated at 100±0.1 °C in a forced-convection oven. Different diameters of α-Fe_2O_3 NPs were obtained at different incubation times of approximately 30 min, 5 h, and 8 h for the three sizes (15, 50, and 78 nm) used in this study. The suspension was centrifuged (Eppendorf centrifuge 5430R, Germany) at 5,000×*g* for 30 min, and the supernatant was discarded. The concentrated α-Fe_2O_3 NPs were stored in deionized (DI) water (Millipore, >18.2 MΩ) at pH 4±0.1 adjusted by hydrochloride acid.

The morphology and particle diameters were examined with a Philips CM-12 TEM operating at an accelerating voltage of 80 kV. Hydrodynamic diameters of α-Fe_2O_3 NPs dispersed in DI water or culture media were determined by a dynamic light scattering (DLS) instrument (Malvern Instruments, Zetasizer Nano, ZS instrument). The concentration of α-Fe_2O_3 NPs in suspension was determined by an Induced Coupled Plasma-Optical Emission Spectrometry (ICP-OES, Thermo iCAP 6300, USA). The concentration of α-Fe_2O_3 NPs was expressed mg/L of ferric ion.

Cell culture

BeWo (b30) cells were obtained from Dr. Erik Rytting (UTMB, Galveston, TX), and used with permission from Dr. Alan Schwartz. Cells were maintained in T-75 flasks (Corning, Manassas, VA) coated with 50 μg/mL human placenta collagen (Sigma Aldrich, St. Louis, MO) as described elsewhere (Bode et al. 2006). Briefly, culture medium was replenished daily with DMEM:F-12 containing 1 % antibiotics (10,000 IU/mL penicillin/10,000 μg/mL streptomycin/25 μg/mL amphotericin B; Cellgro, Manassas, VA), and 15 % fetal bovine serum (Atlanta Biological, Lawrenceville, GA), and incubated in a humidified chamber of 5 % CO_2 in air at 37 °C. Upon 80 % confluence, the cells were subcultured at a 1:10 dilution. Subculturing was accomplished by briefly incubating the cells in Ca^{2+}/Mg^{2+}-free phosphate buffered saline (PBS), followed by a 5-min incubation in 0.25 % trypsin/2.21 mM EDTA in Hanks Balanced Salt Solution (Cellgro, Manassas, VA) until the cells were no longer adherent to the culture plastic as assessed by phase contrast microscopy. The trypsin was neutralized, removed, and the cells were resuspended to the appropriate cell dilution.

NP-containing medium was prepared as described by Koeneman and coworkers (Koeneman, Zhang et al. 2010). Briefly, water-soluble α-Fe_2O_3 at a stock concentration of no less than 2000 mg/L was sonicated with a Fisher Scientific model 100 probe sonic dismembrator at the maximum setting of 28 W (RMS) for no less than 2 min. After applying the NPs to the appropriate volume of medium required to obtain the final working concentration, a second round of sonication, prior to exposure to epithelia was performed according to the aforementioned settings. All NP concentrations used in this study were calibrated to equal the concentration employed during TEER analysis depending on the area of the culture vessel (i.e., 33 μg/mm^2=100 μg/mL in a Transwell® insert).

Transepithelial electrical resistance

Cells were grown on collagen-coated, 0.4 μm pore, 6.5 mm Transwell® Inserts (Corning, Manassas, VA), and were allowed to grow until an intact monolayer formed as described elsewhere (Cartwright et al. 2012). Typically, the monolayer and TEER is established 3 days post-seeding (Cartwright et al. 2012) and this timepoint was used in all experiments reported in this study as "day 0," and the values obtained were in agreement with recent reports (Li et al. 2013). Before measurements were taken, the 24-well plate was set in the dark on an air curtain for 15 min to equilibrate to room temperature. A thermometer was placed in blank well containing 1.5 mL of medium, and only after the medium was room temperature were the measurements taken. Measurements were consistently taken in order. Three different measurements were taken from each insert and averaged. TEER measurements were conducted with an EVOM (World Precision Instruments, Inc., Sarasota, FL) and TPX2 "chopstick" electrodes (World Precision Instruments Inc., Sarasota, FL). Resistance was assessed only after the electrode was calibrated with a CaliCell (World Precision Instruments, Inc., Sarasota, FL) to ensure accurate readings. Background resistance was measured by employing a blank inserts (n=3) with medium

only and no cells. TEER is calculated from the following equation:

$$R_{\mathrm{TEER}} = [R_C\_R_B]\mathrm{X}A$$

Where R_{TEER} is the transepithelial electrical resistance represented in Ω cm^2; R_C is the resistance of the cells in Ω; R_B is the resistance of the blank (Ω); and A is the surface area of the membrane insert (cm^2). There were several populations of "blanks" depending on the experiment; however, control blanks are defined as inserts containing no cells bathed in 300 μL of medium in the apical chamber and 1 mL of medium in the basal chamber. For experiments assessing TEER for NP-treated epithelia, the blank is redefined as an insert containing no cells, but incubated with medium containing the total working concentration of the nanomaterial at a consistent volume in the apical chamber as described earlier in the text (i.e., 300 μL at × μg/mL NPs), and with 1 mL of medium containing no NPs in the basal chamber. In each case, no fewer than three blank inserts were averaged to obtain the "blank" resistance required to calculate TEER values. All TEER values were normalized to percent TEER based on the average percent of the epithelia for 3 consecutive days prior to NP application. NP containing medium was applied once at day 0 to the apical chamber alone. Each insert received the same amount of medium; The apical chamber contained 300 μL and the basal chamber contained 1 mL of culture medium. Cell culture medium was replenished every 24 h. Each experiment was repeated at least three times where (n=3).

ROS analysis

BeWo cells were seeded on human placenta collagen-coated glass bottom dishes (Sigma Aldrich, St. Louis, MO; MatTek, Ashland, MA) and grown for 3 days corresponding to the maximal TEER as described in the sections in the above text (i.e., the "day 0" timepoint). The cell permeate reactive oxygen species indicator, H_2DCFDA (Molecular Probes; D-399) with aid from 0.02 % Pluronic F-127, was bath-applied to the epithelia. Once the reduced fluorescein derivative enters the cell, esterases can cleave acetate groups and the probe can be oxidized by ROS. Upon oxidation H_2DCFDA is converted to 2′,7′-dicholorofluorescein and exhibits a bright green fluorescence. This cocktail was applied to epithelia for 30 min in a humified incubator, subsequently washed several times in pre-equilibrated Ca^{2+}/Mg^{2+}-containing PBS (37 °C), and imaged as detailed in the preceding text. A positive control for reactive oxygen species was employed by applying 5 μM H_2O_2 in standard cell culture medium overnight (8 h) and later assessing fluorescent cells. No fewer than five randomly chosen fields of view were imaged and the entire field of view scored for fluorescence in each specimen. Each experiment was repeated three times where (n=3).

Live/dead analysis

The live/dead cytotoxicity assay (Molecular Probes; L-3224) was used to identify dead cells. Briefly, the red-fluorescent ethidium homodimer-1 is excluded by intact cells indicative of cell viability. However, when membrane integrity is compromised during cellular death, ethidium binds to nuclear DNA and undergoes an increase in intensity (40-fold increase in fluorescence; Gaugain et al. 1978). Thus, cells that are dead have intense nuclear fluorescence. To indentify dead cells in the epithelium, BeWo cells were seeded on human placenta collagen-coated glass bottom dishes (MatTek, Ashland, MA) until confluence. Ethidium was made 10 μM in standard culture medium and the cells were incubated for 40 min in a humified chamber at 37 °C. The cells were subsequently washed in Ca^{2+}/Mg^{2+}-containing PBS to remove any unbound ethidium, standard culture medium was replaced, and the plates were immediately imaged in the dark on a Nikon Eclipse TE300 inverted microscope equipped with a stage warmer and a Hamamatsu Orca CCD camera. Each experiment was repeated three times where (n=3).

Transmission electron microscopy

All reagents and materials were purchased from Electron Microscopy Sciences (Hatfield, PA) unless otherwise indicated. In all cases describing cytological fixation, EM grade formaldehyde and glutaraldehyde were opened and used fresh from vials stored under N_2 gas. Cells were seeded on collagen-coated aclar and cultured as described in the preceding text. To obtain resin-embedded monolayers, the cells were cytologically fixed for 2 h in sodium cacodylate buffer (pH 7.2) made 2 % with formaldehyde/2 % glutaraldehyde. The specimens were washed extensively to remove the excess

fixative and subsequently post-fixed in 1 % OsO_4 for 1 h in the dark at room temperature. After extensive washes in Nanopure™ water, the cells were incubated overnight in 0.5 % uranyl acetate in Nanopure™ water at 4 °C. Specimens were dehydrated in an increasing graded series of ethanol and infiltrated with Spur's embedding medium and polymerized overnight at 60 °C. Seventy nanometer sections (corresponding to silver interference patterns) were cut on a Leica Ultracut E equipped with a diamond knife (Diatome, Hatfield, PA), and collected on formvar-coated, carbon-stabilized copper grids. The section-containing grids were stained with uranyl acetate and Sato's lead citrate, allowed to air dry overnight, and imaged on a Phillips CM-12 TEM fitted with a Gatan 791 CCD camera.

Scanning electron microscopy

Poly-D-lysine-coated cover slips were purchased (BD Bioscience, San Jose, CA) and subsequently coated with human placenta collagen at 5 μg/cm^2. The cover slips were extensively washed in PBS and BeWo cells were seeded at 4×10^5 cells/mL. Epithelia were washed briefly with PBS and cytologically fixed for 30 min in 100 mM sodium cacodylate buffer (pH 7.2) made 2 % formaldehyde/2 % glutaraldehyde at room temperature. Specimens were washed through several changes of sodium cacodylate buffer (pH 7.2) and post-fixed in 1 % OsO_4 for 60 min in the dark. Following post-fixation, the epithelia were washed with Nanopure™ water and dehydrated in an increasing graded ethanol series. Samples were dried through the critical point of CO_2 (Balzers), mounted on aluminum stubs, and sputter coated with approximately 5 nm of palladium-gold in a vacuum (Technicks Hummer II). Images were collected on a JOEL JSM-6300 scanning electron microscopy equipped with an IXRF digital imaging system. Each experiment was repeated a minimum of four times (n=4)

Cytochalasin D treatment to prevent actin-mediated endocytosis

Cytochalasin D binds to g-actin and prevents f-actin formation and subsequent actin-mediated endocytosis. Cytochalasin D was purchased from Sigma Aldrich and made 10 mM in cell culture tested dimethylsulfoxide (ATCC). This stock dilution was stored at -20 °C in 10 μL aliquots and thawed just prior to use. Prior to NP treatment, a dose response analysis (unpublished data) for Cytochalasin D was conducted and it was found that application of 1 μM Cytochalasin D 30 min prior to, and during the duration of NP incubation (≥8 h) resulted in a loss of f-actin, but maintained cellular viability. The final working concentration of 1 μM was employed in all subsequent studies.

Immunocytochemistry

Unless otherwise stated, all reagents used for immunocytochemistry were purchased from Sigma Aldrich (St. Louis, MO). Confluent epithelia were treated and maintained as replicate samples at their respective time points. The epithelia were briefly washed in PBS equilibrated to 37 °C, and subsequently cytologically fixed in 100 mM PBS made 2 % with formaldehyde prepared fresh from paraformaldehyde for 30 min at room temperature. Epithelia were permeabilized with an intracellular buffer (ICB) made 2 % with formaldehyde and 0.1 % Triton X-100 for 30 min at room temperature in the dark. ICB contains the following: 100 mM KCl, 5 mM $MgCl_2$, and 20 mM HEPES™ (pH 6.8). The epithelia were washed three times for 15 min per wash in ICB made 1 % with bovine serum albumin (ICB-BSA) at room temperature. After this blocking step, the primary antibody (anti-ZO-1, Invitrogen ZO1-1A12 [formerly from Zymed]) was applied at a 1:500 dilution in an antibody dilution buffer (ICB modified to contain 0.1 % Tween-20 and 1 % non-fat dry milk) and incubated overnight at 4 °C. The following day the epithelia were washed three times for 15 min each in ICB-BSA. The fluorophore-conjugated secondary antibody used in this study, which permitted visualization of the primary antibody, was goat-anti-mouse Alexa-488. The secondary antibody was used at a 1:500 dilution in antibody dilution buffer and incubated overnight at 4 °C. The following day, the epithelia were washed three times for 15 min each in ICB. Visualization of the nuclei was accomplished by employing DAPI (Molecular Probes) diluted in ICB for 15 min. The cover slips were subsequently mounted on slides in drops of Vectashield (Vector Labs) and sealed with optically clear nail polish. Images were collected with a Leica SP5 laser scanning confocal microscope housed in the W.M. Keck Bioimaging Facility at Arizona State University. The images

represent 0.4 μm optical Z-sections obtained through the entire volume of the cells for confocal analysis. Optical sections were reconstructed using Leica Imaging Software to represent a maximum projection image. The images shown are representative of four independent experiments where $n=3$.

Microarray analysis

mRNA isolation

All plastic cultureware employed during microarray analysis was certified as "Nuclease-free." Messenger RNA (message) was isolation by the Purelink® RNA method (Ambion) according to the manufacturer's instructions. Briefly, three confluent 60 mm^2 culture plates for each condition (i.e., untreated, 15 nm treated, and 78 nm treated) for a total of nine plates were washed in ice-cold PBS, scrapped, at the respective times, with a rubber policeman and collected in ice-cold PBS. PBS was removed, replaced with lysis buffer, and mechanically disrupted with five strokes of a Dounce homogenizer. Message was subsequently isolated on membranes and eluted into collection tubes through the use of TE buffer. RNA was stored in a mechanical freezer at -80 °C until use.

aRNA amplification and microarray analysis

Messenger RNA was thawed on ice and analyzed for total RNA content with a Nanodrop™ spectrophotometer. RNA was aliquotted into non-stick PCR tubes at a total concentration of 1,000 ng per tube. Reverse transcription "master mix" was prepared and DNA was transcribed in a hybridization oven at 42 °C for 2 h. Complementary DNA (cDNA) was subsequently prepared at 16 °C for 2 h. The cDNA was purified and transcribed into amino allyl RNA. The aRNA was purified and the yield was assessed. Depending on the specimen Alexa-fluor 555 or Alexa-fluor 647 was coupled to the aRNA, the former representing the untreated specimens, while the latter represents the NP-treated specimens. Dye-coupled aRNA was purified, fragmented and equal concentrations of untreated and treated aRNA was pooled. The samples were subsequently hybridized on Agilent Human 4×44 K arrays at 60 °C for 16 h, scanned, and analyzed with GeneSpring (Agilent Technologies, Inc., Santa Clara, CA). Data represent biological replicates conducted on the same day.

Q-PRC analysis

The same mRNA that was employed for microarray analysis was used to confirm relative fold-changes for the *CASP8* and *TNFR12A* genes. Reverse transcription was accomplished with the qScript cDNA synthesis kit according to the manufacturer's instructions (Quanta Biosciences, Gaithersburg, MD). This cDNA was used as a template for quantative PCR analysis through the use of Brilliant III CYBR® Green (Agilent Technologies, Inc., Santa Clara, CA). Briefly, equal amount of template were amplified and fluorescence was monitored and analyzed by the ΔΔCt method (Livak and Schmittgen 2001). The housekeeping gene, *TUBA1A*, which encodes the protein α-tubulin, was used to normalize data. The *CASP8* amplicon was generated with primers corresponding to the forward: CAGTGAAGAT CTGGCCTCCC and reverse: TGCGGAATGTAGTC CAGGCT sequences. The *TNFR12A* gene product was amplified with forward AAGGAACTGCAGCATTTG CA and reverse CCTCTAGGAAGGAGGGCACC primers according to the manufacturer's recommendations (Integrated DNA Technologies, San Diego, CA). Data represent biological replicates conducted on the same day. Error is shown as mean±SD.

Data analysis

In this manuscript an independent experiment is defined as three or more technical replicates conducted on the same day. Unless otherwise stated, all data represent at least three independent experiments conducted on different days. Student's *t*-test was performed through the use of GraphPad software and a p value of ≤ 0.05 was considered statistically significant. Error was calculated in Excel and is shown as mean±SEM. In some cases error bars appear smaller than the data point marker. All comparisons are made between untreated and NP-treated epithelia at their respective time points unless otherwise indicated.

Microarray data was analyzed through the use of GeneSpring and the data appears as three biological replicates conducted on the same day. Only those genes that whose change represented $p \leq 0.05$ were considered for subsequent analysis. Quantitative PCR analysis was

conducted on the same day as three technical replicates. Both microarray and QPCR are shown as mean±SD.

Acknowledgments The authors are indebted to Professor Erik Rytting at UTMB for providing the BeWo b30 cell line employed during this study. Professor Kaushal Rege and Dr. Thrimoorthy Potta are greatly thanked for their helpful discussions of this research. The authors thank Dr. Scott Bingham for his unique willingness to provide assistance in the DNA Core Facility at Arizona State University. The authors thank Mr. David Lowry for his patience training JJF on the scanning scope. All imaging data was procured in the W.M. Keck Bioimaging Facility at Arizona State University. JJF is supported in part by the McKee Award funded by the Delta Sigma Phi Foundation, and the Dr. and Mrs. John Maher Scholarship. This study was partially supported by the US Environmental Protection Agency Science to Achieve Results Program grant RD-83385601 and National Science Foundation Grant CBET-1235166.

Competing interests The authors declare no competing interests.

References

Amstad E, Textor M, Reimhult E. Stabilization and functionalization of iron oxide nanoparticles for biomedical applications. Nanoscale. 2011;3(7):2819–43.

Anderson JM, Van Itallie CM, Peterson MD, Stevenson BR, Carew EA, Mooseker MS. ZO-1 mRNA and protein expression during tight junction assembly in Caco-2 cells. J Cell Biol. 1989;109(3):1047–56.

Aplin J. The cell biology of human implantation. Placenta. 1996;17(5):269–75.

Bement WM, Forscher P, Mooseker MS. A novel cytoskeletal structure involved in purse string wound closure and cell polarity maintenance. J Cell Biol. 1993;121(3):565–78. Epub 1993/05/01.

Berryman M, Gary R, Bretscher A. Ezrin oligomers are major cytoskeletal components of placental microvilli: a proposal for their involvement in cortical morphogenesis. J Cell Biol. 1995;131(5):1231–42.

Bhabra G, Sood A, Fisher B, Cartwright L, Saunders M, Evans WH, et al. Nanoparticles can cause DNA damage across a cellular barrier. Nat Nanotechnol. 2009;4(12):876–83.

Blowes DW, Ptacek CJ, Jambor JL. In-situ remediation of Cr (VI)-contaminated groundwater using permeable reactive walls: laboratory studies. Environ Sci Technol. 1997;31(12):3348–57.

Blume LF, Denker M, Gieseler F, Kunze T. Temperature corrected transepithelial electrical resistance (TEER) measurement to quantify rapid changes in paracellular permeability. Pharmazie. 2010;65:19–24.

Bode CJ, Jin H, Rytting E, Silverstein PS, Young AM, Audus KL. In vitro models for studying trophoblast transcellular transport. Methods Mol Med. 2006;122:225–39. Epub 2006/03/04.

Buyukhatipoglu K, Clyne AM. Superparamagnetic iron oxide nanoparticles change endothelial cell morphology and mechanics via reactive oxygen species formation. J Biomed Mater Res A. 2011;96(1):186–95.

Cartwright L, Poulsen MS, Nielsen HM, Pojana G, Knudsen LE, Saunders M, et al. In vitro placental model optimization for nanoparticle transport studies. Int J Nanomedicine. 2012;7:497–510. Epub 2012/02/16.

Claude P. Morphological factors influencing transepithelial permeability: A model for the resistance of thezonula occludens. J Membr Biol. 1978;39(2–3):219–32.

Denker HW. Implantation: a cell biological paradox. J Exp Zool. 1993;266(6):541–58. Epub 1993/09/01.

Ehrenberg MS, Friedman AE, Finkelstein JN, Oberdörster G, McGrath JL. The influence of protein adsorption on nanoparticle association with cultured endothelial cells. Biomaterials. 2009;30(4):603–10.

Ellis RE, Yuan J, Horvitz H. Mechanisms and functions of cell death. Annu Rev Cell Biol. 1991;7(1):663–98.

Faust JJ, Zhang W, Koeneman BA, Chen Y, Capco DG. Commenting on the effects of surface treated- and non-surface treated TiO(2) in the Caco-2 cell model. Part Fibre Toxicol. 2012;9:42. Epub 2012/11/14.

Fischer U, Jänicke R, Schulze-Osthoff K. Many cuts to ruin: a comprehensive update of caspase substrates. Cell Death Differ. 2003;10(1):76–100.

Fulda S, Debatin K. Extrinsic versus intrinsic apoptosis pathways in anticancer chemotherapy. Oncogene. 2006;25(34):4798–811.

Furuse M, Itoh M, Hirase T, Nagafuchi A, Yonemura S, Tsukita S. Direct association of occludin with ZO-1 and its possible involvement in the localization of occludin at tight junctions. J Cell Biol. 1994;127(6):1617–26.

Gaugain B, Barbet J, Capelle N, Roques BP, Le Pecq JB, Le Bret M. DNA bifunctional intercalators. 2. Fluorescence properties and DNA binding interaction of an ethidium homodimer and an acridine ethidium heterodimer. Appendix: Numerical solution of McGhee and von Hippel equations for competing ligands. Biochemistry. 1978;17:5078–88.

Grummer R, Hohn HP, Mareel MM, Denker HW. Adhesion and invasion of three human choriocarcinoma cell lines into human endometrium in a three-dimensional organ culture system. Placenta. 1994;15(4):411–29. Epub 1994/06/01.

Guo H, Stüben D, Berner Z. Removal of arsenic from aqueous solution by natural siderite and hematite. Appl Geochem. 2007;22(5):1039–51.

Gupta AK, Gupta M. Synthesis and surface engineering of iron oxide nanoparticles for biomedical applications. Biomaterials. 2005;26(18):3995–4021.

Gupta AK, Naregalkar RR, Vaidya VD, Gupta M. Recent advances on surface engineering of magnetic iron oxide nanoparticles and their biomedical applications. Nanomedicine (Lond). 2007;2:23–39.

Hannan NJ, Paiva P, Dimitriadis E, Salamonsen LA. Models for study of human embryo implantation: choice of cell lines? Biol Reprod. 2010;82(2):235–45.

He YT, Wan J, Tokunaga T. Kinetic stability of hematite nanoparticles: the effect of particle sizes. J Nanoparticle Res. 2008;10(2):321–32.

Heintzelman MB, Hasson T, Mooseker MS. Multiple unconventional myosin domains of the intestinal brush border cytoskeleton. J Cell Sci. 1994;107(12):3535–43.

Hidalgo IJ, Raub T, Borchardt R. Characterization of the human colon carcinoma cell line (Caco-2) as a model system for intestinal epithelial permeability. Gastroenterology. 1989;96(3):736.

Huppertz B. Nanoparticles: Barrier thickness matters. Nat Nanotechnol. 2011;6(12):758–9.

John NJ, Linke M, Denker HW. Quantitation of human choriocarcinoma spheroid attachment to uterine epithelial cell monolayers. In Vitro Cell Dev Biol Anim. 1993;29A(6):461–8. Epub 1993/06/01.

Jovov B, Wills NK, Lewis SA. A spectroscopic method for assessing confluence of epithelial cell cultures. Am J Physiol. 1991;261:C1196–203.

Kalive M, Zhang W, Chen Y, Capco DG. Human intestinal epithelial cells exhibit a cellular response indicating a potential toxicity upon exposure to hematite nanoparticles. Cell Biol Toxicol. 2012;28(5):343–68. Epub 2012/08/21.

Kievit FM, Zhang M. Surface engineering of iron oxide nanoparticles for targeted cancer therapy. Acc Chem Res. 2011;44(10):853–62.

King BF. Comparative studies of structure and function in mammalian placentas with special reference to maternal-fetal transfer of iron. Am Zool. 1992;32(2):331–42.

Koeneman BA, Zhang Y, Hristovski K, Westerhoff P, Chen Y, Crittenden JC, et al. Experimental approach for an< i> in vitro</i> toxicity assay with non-aggregated quantum dots. Toxicol In Vitro. 2009;23(5):955–62.

Koeneman BA, Zhang Y, Westerhoff P, Chen Y, Crittenden JC, Capco DG. Toxicity and cellular responses of intestinal cells exposed to titanium dioxide. Cell Biol Toxicol. 2010;26(3):225–38.

Kokkinos MI, Murthi P, Wafai R, Thompson EW, Newgreen DF. Cadherins in the human placenta–epithelial-mesenchymal transition (EMT) and placental development. Placenta. 2010;31(9):747–55. Epub 2010/07/28.

Kreuter J. Drug targeting with nanoparticles. Eur J Drug Metab Pharmacokinet. 1994;19(3):253–6.

Kulvietis V, Zalgeviciene V, Didziapetriene J, Rotomskis R. Transport of nanoparticles through the placental barrier. Tohoku J Exp Med. 2011;225(4):225–34.

Lee N, Tong MK, Leung PP, Chan VW, Leung S, Tam P-C, et al. Kidney claudin-19: localization in distal tubules and collecting ducts and dysregulation in polycystic renal disease. FEBS Lett. 2006;580(3):923.

Li H, van Ravenzwaay B, Rietjens IM, Louisse J. Assessment of an in vitro transport model using BeWo b30 cells to predict placental transfer of compounds. Arch Toxicol. 2013. Epub 2013/05/22.

Livak KJ, Schmittgen TD. Analysis of relative gene expression data using real-time quantitative PCR and the 2(-Delta Delta C(T)) Method. Methods (San Diego, Calif). 2001;25(4):402–8. Epub 2002/02/16.

Mahmoudi M, Sant S, Wang B, Laurent S, Sen T. Superparamagnetic iron oxide nanoparticles (SPIONs): development, surface modification and applications in chemotherapy. Adv Drug Deliv Rev. 2011;63(1):24–46.

Maiorano G, Sabella S, Sorce B, Brunetti V, Malvindi MA, Cingolani R, et al. Effects of cell culture media on the dynamic formation of protein− nanoparticle complexes and influence on the cellular response. ACS Nano. 2010;4(12):7481–91.

Mardon H, Grewal S, Mills K. Experimental models for investigating implantation of the human embryo. Semin Reprod Med. 2007;25:410–7.

Matter K, Aijaz S, Tsapara A, Balda MS. Mammalian tight junctions in the regulation of epithelial differentiation and proliferation. Curr Opin Cell Biol. 2005;17(5):453–8.

Menezes V, Malek A, Keelan AJ. Nanoparticulate drug delivery in pregnancy: placental passage and fetal exposure. Curr Pharm Biotechnol. 2011;12(5):731–42.

Mishra B, Patel BB, Tiwari S. Colloidal nanocarriers: a review on formulation technology, types and applications toward targeted drug delivery. Nanomedicine Nanotechnol Biol Med. 2010;6(1):9–24.

Mooseker MS. Organization, chemistry, and assembly of the cytoskeletal apparatus of the intestinal brush border. Annu Rev Cell Biol. 1985;1(1):209–41.

Morck TJ, Sorda G, Bechi N, Rasmussen BS, Nielsen JB, Ietta F, et al. Placental transport and in vitro effects of Bisphenol A. Reprod Toxicol (Elmsford, NY). 2010;30(1):131–7. Epub 2010/03/11.

Mukherjee T, Squillantea E, Gillespieb M, Shao J. Transepithelial electrical resistance is not a reliable measurement of the Caco-2 monolayer integrity in Transwell. Drug Deliv. 2004;11:11–8.

Mutch DM, Berger A, Mansourian R, Rytz A, Roberts M-A. The limit fold change model: a practical approach for selecting differentially expressed genes from microarray data. BMC Bioinforma. 2002;3(1):17.

Nagata S. Apoptosis by Death Factor Review. Cell. 1997;88(355–365):392.

Pattillo RA, Gey GO. The establishment of a cell line of human hormone-synthesizing trophoblastic cells in vitro. Cancer Res. 1968;28(7):1231–6. Epub 1968/07/01.

Penners N, Koopal L. Preparation and optical properties of homodisperse haematite hydrosols. Colloids Surf. 1986;19(4):337–49.

Pietroiusti A, Campagnolo L, Fadeel B. Interactions of engineered nanoparticles with organs protected by internal biological barriers. Small. 2013;9:1557–72.

Pijnenborg R. Trophoblast invasion and placentation in the human: morphological aspects. Trophoblast Invasion and Endometrial Receptivity: Springer; 1990. p. 33–47.

Quackenbush J. Microarray data normalization and transformation. Nat Genet. 2002;32:496–501.

Rampon C, Bouillot S, Climescu-Haulica A, Prandini M-H, Cand F, Vandenbrouck Y, et al. Protocadherin 12 deficiency alters morphogenesis and transcriptional profile of the placenta. Physiol Genomics. 2008;34(2):193–204.

Reed JC. Mechanisms of apoptosis. Am J Pathol. 2000;157(5):1415–30.

Rytting E, Audus KL. Novel organic cation transporter 2-mediated carnitine uptake in placental choriocarcinoma (BeWo) cells. J Pharmacol Exp Ther. 2005;312(1):192–8. Epub 2004/08/19.

Rytting E, Audus KL. Effects of low oxygen levels on the expression and function of transporter OCTN2 in BeWo cells. J Pharm Pharmacol. 2007;59(8):1095–102. Epub 2007/08/30.

Rytting E, Audus KL. Contributions of phosphorylation to regulation of OCTN2 uptake of carnitine are minimal in BeWo

cells. Biochem Pharmacol. 2008;75(3):745–51. Epub 2007/11/06.

Saunders M. Transplacental transport of nanomaterials. Wiley interdisciplinary reviews. Nanomedicine Nanobiotechnol. 2009;1(6):671–84. Epub 2010/01/06.

Semmler-Behnke M, Fertsch S, Schmid G, Wenk A, Kreyling WG. Uptake of 1.4 nm versus 18 nm gold nanoparticles in secondary target organs is size dependent in control and pregnant rats after intratracheal or intravenous application. EuroNanoForum 2007. 2007:102.

Semmler–Behnke M, Kreyling WG, Lipka J, Fertsch S, Wenk A, Takenaka S, et al. Biodistribution of 1.4– and 18–nm Gold Particles in Rats. Small. 2008;4(12):2108–11.

Silverstein SC, Steinman RM, Cohn ZA. Endocytosis. Annu Rev Biochem. 1977;46(1):669–722.

Sood A, Salih S, Roh D, Lacharme-Lora L, Parry M, Hardiman B, et al. Signalling of DNA damage and cytokines across cell barriers exposed to nanoparticles depends on barrier thickness. Nat Nanotechnol. 2011;6(12):824–33.

Stevenson BR, Siliciano JD, Mooseker MS, Goodenough DA. Identification of ZO-1: a high molecular weight polypeptide associated with the tight junction (zonula occludens) in a variety of epithelia. J Cell Biol. 1986;103(3):755–66.

Takeda K, Suzuki K-I, Ishihara A, Kubo-Irie M, Fujimoto R, Tabata M, et al. Nanoparticles transferred from pregnant mice to their offspring can damage the genital and cranial nerve systems. J Health Sci. 2009;55(1):95–102.

Thorburn A. Death receptor-induced cell killing. Cell Signal. 2004;16(2):139–44.

van der Ende A, du Maine A, Simmons CF, Schwartz AL, Strous GJ. Iron metabolism in BeWo chorion carcinoma cells. Transferrin-mediated uptake and release of iron. J Biol Chem. 1987;262(18):8910–6. Epub 1987/06/25.

van der Ende A, du Maine A, Schwartz AL, Strous GJ. Modulation of transferrin-receptor activity and recycling after induced differentiation of BeWo choriocarcinoma cells. Biochem J. 1990;270(2):451–7. Epub 1990/09/01.

Verma A, Stellacci F. Effect of surface properties on nanoparticle–cell interactions. Small. 2010;6:12–21.

Wahajuddin SA. Superparamagnetic iron oxide nanoparticles: magnetic nanoplatforms as drug carriers. Int J Nanomedicine. 2012;7:3445.

Westerhoff P, Zhang Y, Crittenden J, Chen Y. Properties of commercial nanoparticles that affect their removal during water treatment. Nanoscience and Nanotechnology: Environmental and Health Impacts NJ: John Wiley and Sons. 2008:71–90.

Wice B, Menton D, Geuze H, Schwartz AL. Modulators of cyclic AMP metabolism induce syncytiotrophoblast formation< i> in vitro</i> Exp Cell Res. 1990;186(2):306–16.

Wu C, Yin P, Zhu X, OuYang C, Xie Y. Synthesis of hematite (α-Fe2O3) nanorods: diameter-size and shape effects on their applications in magnetism, lithium ion battery, and gas sensors. J Phys Chem B. 2006;110(36):17806–12.

Yamashita K, Yoshioka Y, Higashisaka K, Mimura K, Morishita Y, Nozaki M, et al. Silica and titanium dioxide nanoparticles cause pregnancy complications in mice. Nat Nanotechnol. 2011;6(5):321–8.

Zhang W, Kalive M, Capco DG, Chen Y. Adsorption of hematite nanoparticles onto Caco-2 cells and the cellular impairments: effect of particle size. Nanotechnology. 2010;21(35):355103. Epub 2010/08/10.

Zhang W, Stack AG, Chen Y. Interaction force measurement between< i> E. coli</i> cells and nanoparticles immobilized surfaces by using AFM. Colloids Surf B: Biointerfaces. 2011;82(2):316–24.

Zhang W, Crittenden J, Li K, Chen Y. Attachment Efficiency of Nanoparticle Aggregation in Aqueous Dispersions: Modeling and Experimental Validation. Environ Sci Technol. 2012a;46(13):7054–62.

Zhang W, Hughes J, Chen Y. Impacts of hematite nanoparticle exposure on biomechanical, adhesive, and surface electrical properties of Escherichia coli cells. Appl Environ Microbiol. 2012b;78(11):3905–15.

Zhou F, Kotru S, Pandey R. Pulsed laser-deposited ilmenite–hematite films for application in high-temperature electronics. Thin Solid Films. 2002;408(1):33–6.